University of Glasgow

DEPARTMENT OF

AEROSPACE ENGINEERING

Numerical Simulation of High-Speed Unsteady Flows over Axisymmetric Spiked Bodies

D.Feszty, K.J. Badcock, B.E. Richards

Aero Report 9903

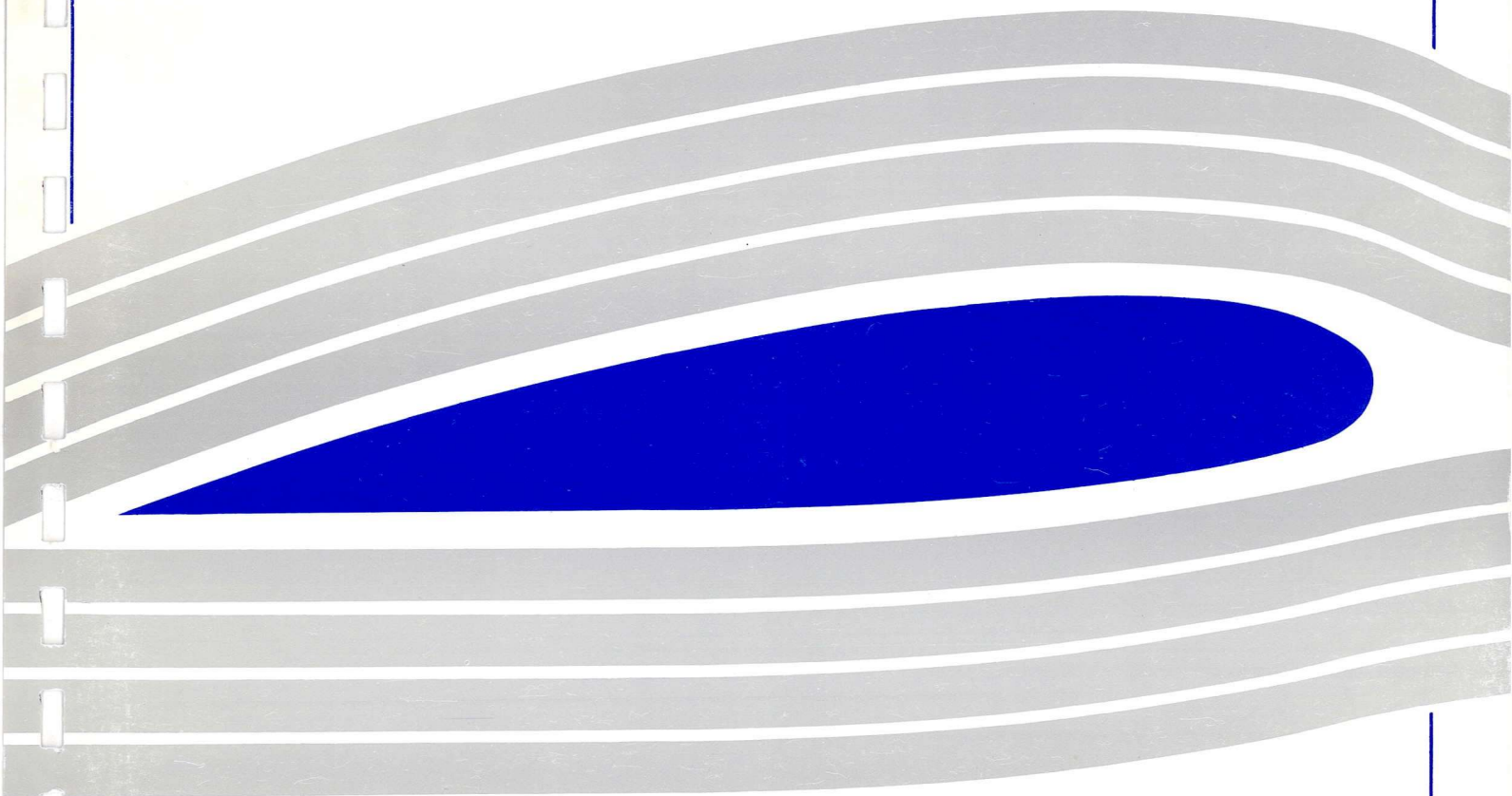

Numerical Simulation of High-Speed Unsteady Flows over Axisymmetric Spiked Bodies

D.Feszty, K.J. Badcock, B.E. Richards

Aero Report 9903

Numerical Simulation of High-Speed Unsteady Flows over Axisymmetric Spiked Bodies

D. Feszty, K.J. Badcock, B.E. Richards

Aero Report 9903,
Department of Aerospace Engineering,
University of Glasgow,
Glasgow, G12 8QQ, U.K.

March 18, 1999

Abstract

The present paper reports some preliminary numerical results for the supersonic/hypersonic unsteady flow over a family of spiked blunt bodies. Axisymmetric compressible Navier-Stokes equations are solved using a high- resolution unfactored implicit upwind Roe's scheme and a time-accurate pseudo-time method is employed for advancing in time. Unsteady flow arising at Mach 2.21 and Mach 6.00 around the spiked 50^o, 70^o cone and cylinder are simulated and the computational results are compared with measurements. The study on these simple shapes for which experimental results are available provides a demonstration that such unsteady flows can be predicted reasonably well and provides confidence that more complex flows such as intake "buzz" and high Reynolds' number ablation can be tackled.

Nomenclature

D	non-dimensional blunt body diameter $\frac{D^*}{D^*}$ [1]
l	non-dimensional spike length $\frac{l^*}{D^*}$ [1]
M	Mach number [1]
Re	Reynolds' number, based on blunt body diameter [1]
CFL	Courant-Friedrichs-Lewy number [1]
V	non dimensional velocity $\frac{V^*}{V_\infty{}^*}$ [1]
p	non-dimensional pressure $\frac{p^*}{\rho_\infty{}^* V_\infty{}^{*2}}$ [1]
t	non-dimensional time $t^* \frac{V_\infty{}^*}{D^*}$ [1]
t_{final}	non-dimensional final real time of an unsteady calculation [1]
T	non-dimensional time period of a cycle [1]
Φ	blunt body half-cone angle [^{o}]
Δp	non-dimensional pressure amplitude [1]
Δt	non-dimensional real time step size in unsteady calculation [1]
ρ	non-dimensional density $\frac{\rho^*}{\rho_\infty{}^*}$ [1]

Suffices

$*$	dimensional quantities
∞	free-stream value

1 Introduction

Numerical simulation of unsteady and high-speed flows is important since their correct solution can save the expense of experiments and in some cases allow the exploration of flow conditions beyond the capabilities of ground-based facilities. High-speed flow around axisymmetric spiked bodies can become unsteady for certain geometries and the proper and accurate prediction of the aerodynamic features is important in order to ensure the correct and safe operation of these vehicles.

The first application where unsteady flow around a spiked-body type shape occurred was an axisymmetric diffuser inlet equipped with conical centerbody (Fig.2a) working at off-design conditions [1] [2]. The observed instability, termed "buzzing", decreased the performance of the propulsion unit and caused serious structural and combustion problems.

The next application of spiked bodies appeared in the early 1950's, when in order to decrease the aerodynamic drag of the ballistic missiles and at the same time to keep the heat transfer rates on the forebody as low as possible a spike was placed at the apex of the blunt forebody (Fig.2b). Several experimental investigations were done at this time [3] [4] [5] [6] [7] [8] to determine the features of the unsteady flow, and two distinct modes were observed, termed oscillation

and pulsation. The oscillation mode was characterised by a change in the shape of the foreshock as it oscillated between a convex and a concave configuration as illustrated in Fig.1a. On the other hand, the pulsation mode was characterised by an excursion between two very different shock envelopes, one consisting of a conical foreshock emanating from the spike tip and intersecting the bow shock created by the blunt body and the second of a single bow shock passing through the spike tip (Fig.1b).

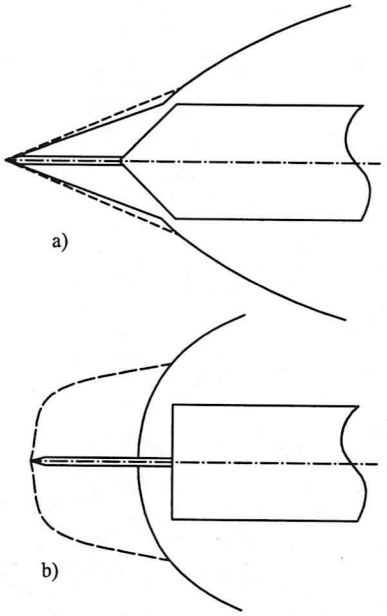

Figure 1: The oscillation (a) and the pulsation mode (b)

Similar unsteady flows may occur around certain families of ablation shapes [9], which are formed during the high Reynolds' number portion of re-entry and when the boundary layer on the hemispherical nose experiences transition from laminar to turbulent flow. This transition causes the peak heat transfer rate to occur away from the stagnation point resulting in a concave conical shape (Fig.2c) which resembles approximately the spiked blunt body. Studies of these shapes [10] [11] indeed show similarity to the flow instabilities observed on spiked blunt bodies. Most recently, the spiked body flows have proved important in connection with the X33-NASP project [12] [13].

The numerical investigations done in this field [14] [15] [16] [17] deal usually with the oscillation mode only or with the flow around spiked blunt bodies with rounded shoulder, such as a spiked hemisphere. Though both oscillation and pulsation modes can take place for these cases, the excursions are more prominent if a sharp-corner cone or even a flat leading edge cylinder is used as the blunt body.

The present paper's aim is to report on numerical

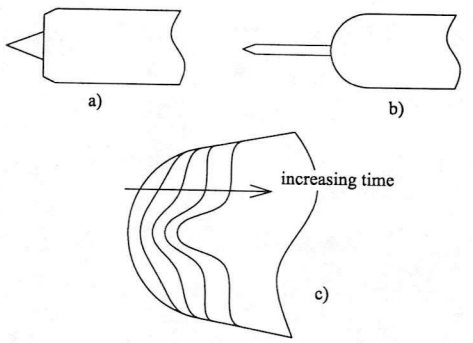

Figure 2: The family of spiked blunt bodies

calculations for simulating the flows over some spiked sharp-corner bodies, which have been investigated experimentally and extensively in [18]. Its scope is to provide confidence in the numerical simulation of such phenomena and to offer some further initial insights into the fundamentals of the high-speed unsteady aerodynamics, which shall be analysed in a later work. The study of these simple shapes also provides a demonstration of the ability of CFD to contribute to the more complex cases such as intake "buzz" on realistic configurations.

2 Test Cases

Reference [18] offers a wide range of results obtained for various spike lengths and cone angles at a supersonic (Mach 2.21) and a hypersonic (Mach 6.00) freestream velocity. For the purposes of the present study, three geometrical configurations were chosen: two representing the ends of the experimentally examined spectrum (50^o and 90^o half-cone angles) and one intermediate (70^o). Each case will be examined at Mach 2.21 and Mach 6.00. The test matrix of the computations is shown in Table 1, and the geometry of the bodies in Fig. 3.

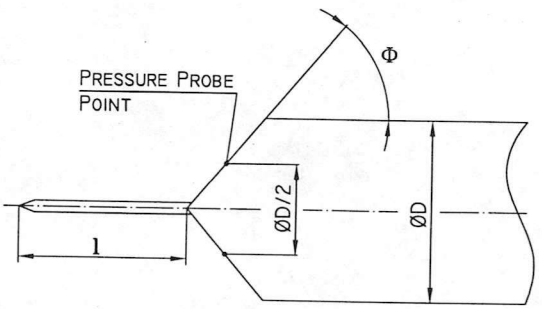

Figure 3: Model geometry

Here, the diameter of the blunt body is set to unit length, whereas the spike's diameter is 6.5 % of this value. The spike ends in a 30^o angle cone and its length is measured from the apex of the blunt body

Φ	l/D	M	Re	expected mode
50^o	0.8	2.21	0.12 million	stable/oscillation
		6.00	0.13 million	stable/oscillation
70^o	0.9	2.21	0.12 million	oscillation/pulsation
		6.00	0.13 million	oscillation
90^o	1.0	2.21	0.12 million	pulsation
		6.00	0.13 million	pulsation

Table 1: The test matrix for the computations

(or from the flat leading edge of the cylinder in the 90^o case). There were two pressure taps placed at a diameter of D/2 on the face of the blunt body (see Fig. 3) in the experiment and the pressure at these points was recorded. In order to gain a comprehensive comparison between the computation and the experiment, the pressure will be monitored at one of these points in the numerical method as well, as the flow is axisymmetric at zero angle of incidence.

3 Simulation Method

3.1 Grid Generation

Two-dimensional, structured, multiblock grids were generated for the above bodies (Fig.4,5,6). The grids had sizes of 20100 cells in 7 blocks for the spiked cones and 15900 cells in 5 blocks for the spiked cylinder. The gridlines were clustered toward the wall of the bodies to enable the viscous calculations. Only every second gridline is shown in the figures.

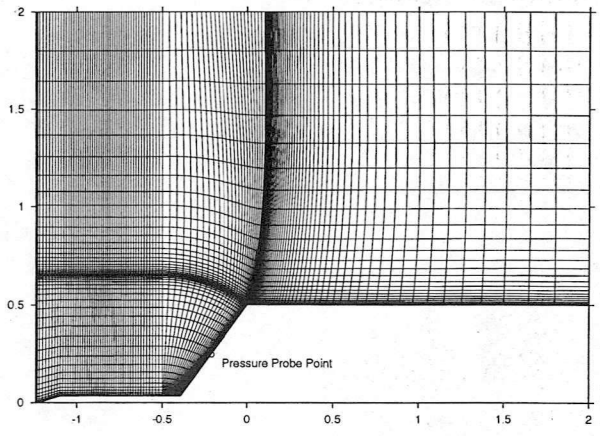

Figure 4: Grid of the spiked 50^o cone

3.2 Numerical Method

The PMB2D code was used for the numerical calculations. This is a generic CFD code developed at the University of Glasgow and used to successfully model

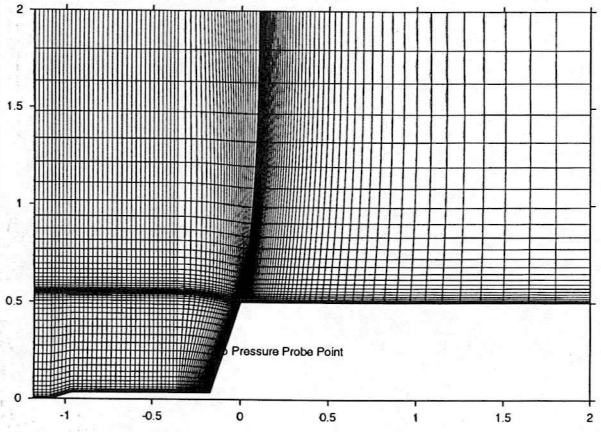

Figure 5: Grid of the spiked 70^o cone

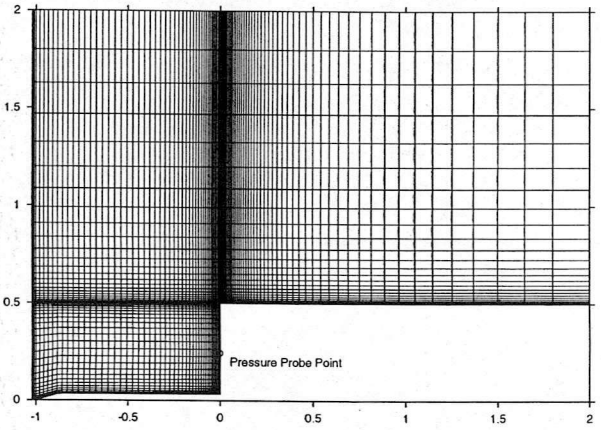

Figure 6: Grid of the spiked cylinder

steady and unsteady flows over aerofoils, wings, bodies, cavities, rearward facing steps, nozzles, jets, etc. in subsonic, transonic and more recently hypersonic flows. It employs a cell-centered finite volume discretisation method to solve the Euler and Navier-Stokes equations. Roe's scheme with MUSCL variable interpolation is used to discretise the convective terms and central differencing for the diffusive terms. A steady state calculation proceeds in two phases, where the freestream starting solution is initially smoothed using an explicit scheme and then an implicit scheme is used to obtain rapid convergence. The linear system arising at each implicit time step is solved using a Generalised Conjugate Gradient method and a BILU factorisation is used as a preconditioner. The code employs a structured multi-block grid system. An important feature of the code is the use of approximate Jacobian matrices for the left hand side of the linear system. The k-ω turbulent model is also implemented. The unsteady part of the code employs an implicit unfactored dual-time method. Here, the rate of convergence between two consecutive real-time steps is monitored by the so-called Pseudo Time Tolerance (PTT), which is defined

as

$$\frac{||\mathbf{w}^{n+1,m+1} - \mathbf{w}^{n+1,m}||_2}{||\mathbf{w}^{n+1,m+1} - \mathbf{w}^{n}||_2}$$

where $\mathbf{w} = (\rho, \rho u, \rho v, \rho E)$ is the vector of conserved variables and $\mathbf{w}^{n,m}$ denotes the m-th pseudo time iterate at the n-th real time level. Based on previous experiences [20] [19] the value of PTT was set on 0.001 for all the results presented in this paper.

In addition, two modifications described in [24] to improve the robustness of the method were also employed in these particular cases. Firstly, a modification of the wall boundary conditions alters negative pressure/density values arising in the ghost cells outside the computational domain to positive ones. This helps the method through the initial phases of the calculation, when the very strong expansion occurring after the sharp-corner cone/cylinder shoulder and resulting in very steep pressure/density gradients at the wall might cause negative pressure/density failure just near the wall. The second modification, Harten's entropy fix, makes Roe's scheme more robust for the resolution of very strong bow shocks arising in front of a blunt body in a hypersonic freestream. Similar to the steady case calculations [24] the activity of these modifications was also monitored in the following.

4 Verification of the Numerical Method

To ensure the reliability of the results and to choose the most suitable grid refinement and real time step size for the calculations, grid dependence and real time step size dependence tests were performed for the spiked 70^o cone and spiked flat nosed cylinder, as these cases were more likely to show clear oscillation/pulsation phenomena. As the driving mechanisms both of the modes are associated with boundary layer separation on the spike [18], all the following calculations were laminar and axisymmetric.

4.1 Grid Dependence Tests

The grid dependence tests were performed on a coarse (number of points in each direction halved) and on a fine grid (number of points in each direction doubled).

Starting with the M=2.21 70^o case, the pressure histories at the probe point are shown in Fig.7. The medium grid history (dashed line) starts with 10 cycles of smaller pressure amplitudes, representing a transient phase required to developing a proper unsteady flow. Then, the cycles suddenly change their amplitude by one order of magnitude, which value corresponds to the pulsation mode in the experiment. The existence of such transient cycles is not in contrary with the experiment, as the samples presented in [18] were also taken after a long time, when the flow had already settled down.

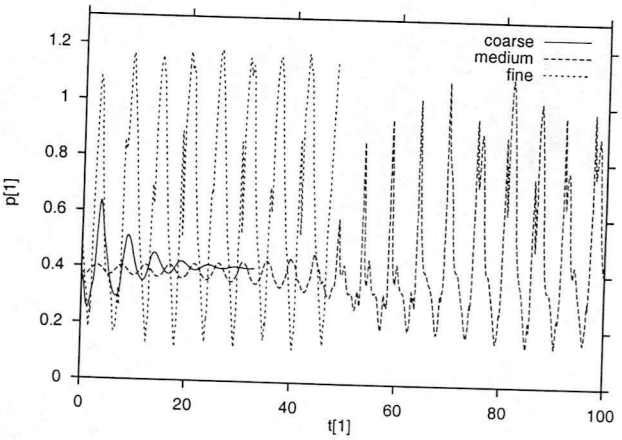

Figure 7: Mach 2.21 spiked 70^o cone: grid dependence test results

On the other hand, the fine grid case history shows an instant development of the pulsation mode not creating any transient cycles at all. This is probably caused by the fact that the pulsation driving mechanism lies in the expected existence of a very fine supersonic jet after the foreshock-aftershock intersection [18]. This, because of its small size and fine nature, could not be immediately developed on the medium grid where a large enough inertia from the previous cycles is necessary to start the pulsation mode whereas a fine grid enables the creation of this small jet crucial for the pulsation driving mechanism immediately. The coarse grid case (solid line) begins with a large amplitude and is gradually damped to a steady state. This probably means that the grid is too coarse to develop the pulsation driving mechanism properly and the unsteadiness of the flow is therefore lost.

In spite of all that, the experiment predicts oscillation to occur at this geometry. However, it will be shown later in section 5.3. that this particular configuration lies very close to the oscillation/pulsation boundary, and that a hysteresis effect in changing the flow mode may indeed result in pulsation at the present spike length.

Continuing with the M=2.21 spiked flat cylinder case, refinement of the grid has no effect on the results in this case, as both the amplitudes and the time periods were basically identical (Fig.8). The only difference is in the graph shapes: compared to the medium grid the pressure plateau is missing in the coarse grid case, whereas it is obviously better pronounced in the fine grid.

In the case of the M=6.00 spiked 70^o cone the coarse grid pressure history shows a similar trend as in the su-

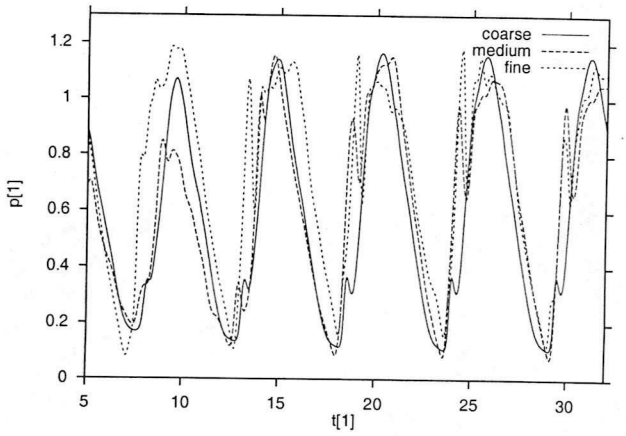

Figure 8: Mach 2.21 spiked cylinder: grid dependence test results

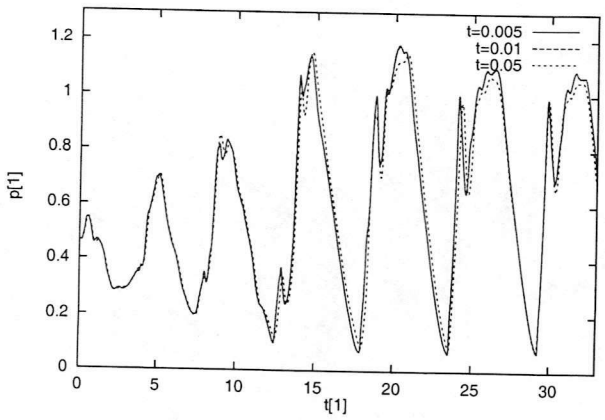

Figure 11: Mach 2.21 spiked cylinder: real time step dependence test results

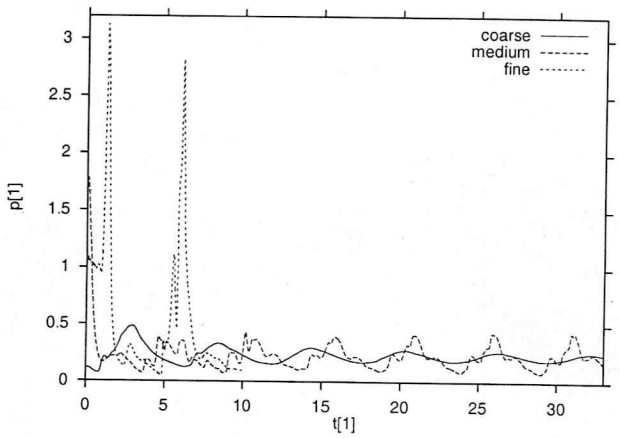

Figure 9: Mach 6.00 spiked 70^o cone: grid dependence test results

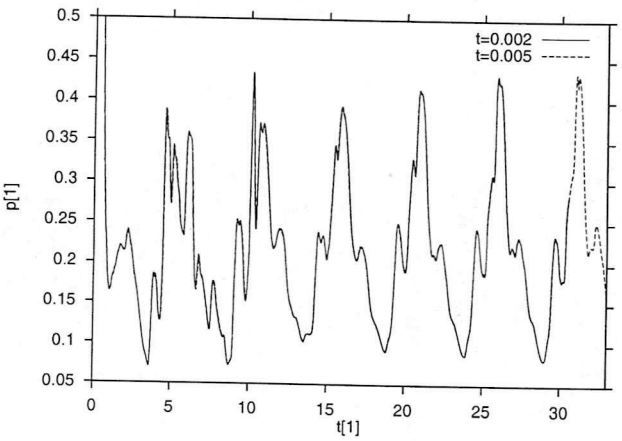

Figure 12: Mach 6.00 spiked 70^o cone: real time step dependence test results

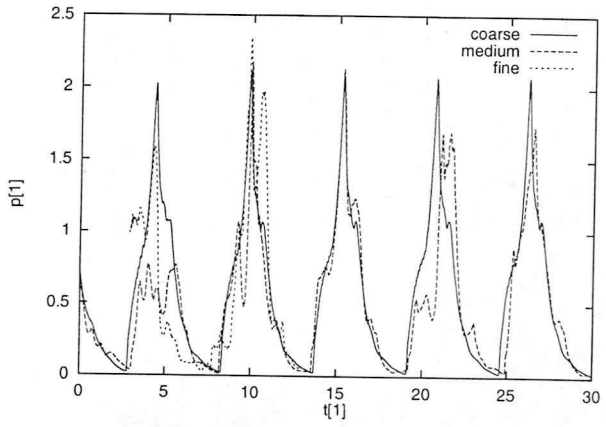

Figure 10: Mach 6.00 spiked cylinder: grid dependence test results

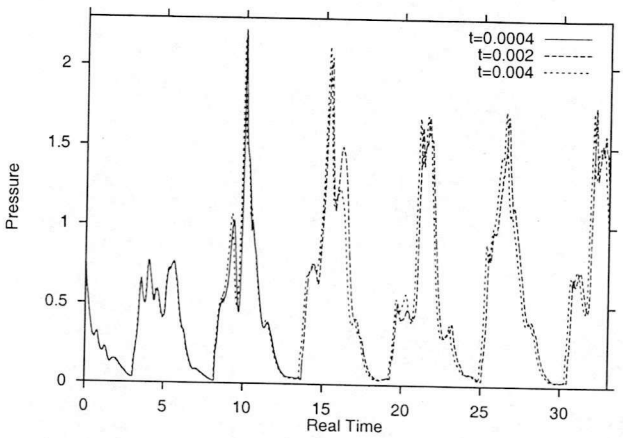

Figure 13: Mach 6.00 spiked cylinder: real time step dependence test results

personic case (Fig.9), starting with a larger amplitude than the medium grid case and gradually damped in time. On the other hand, the fine grid history seems to yield very large overshoots corresponding rather to pulsation. In this case this result could not be explained even by the hysteresis effect, as pulsation did not occur at all at this configuration in the experiment.

In the case of the hypersonic spiked cylinder the time periods of both of the coarse and the fine grid pressure histories are identical with that of the medium one (Fig.10), but they predict slightly higher amplitudes. However, the trends are very similar, characterised by sharp peaks, and an obviously poorer resolution of detail on the coarse grid cycles.

In general, there is a clear indication from the above tests that medium grids are sufficient for obtaining reasonable results. They provide cheaper calculation than the fine grids (including the M=2.21 70^o case, where its time span must be twice as high as the fine ones) and therefore these grids will be used in the following calculations.

4.2 Real Time Step Dependence Tests

The size of the real time step was decreased to half and tenth of the original values, which were 0.05 in the supersonic and 0.004 (0.005 for the 70^o cone) in the hypersonic cases. These values represented the maximum possible real time step sizes and as the pressure histories for all four cases (Figs.11- 13) show that time step size has no effect on the results, the maximum values were used in the following calculations.

5 Computation Results and Validation

5.1 Spiked 50^o Cone at Mach 2.21

Slight unsteadiness was obtained in these calculations. The initial steady state was reached after 1400 explicit steps using CFL=0.4 and 400 implicit steps with CFL=10 (1400/0.4+400/10 in the following) and then the unsteady calculation was advanced in time with a real time step size of Δt=0.05 up to the final time of t_{final}=30. The pressure history at the probe point is shown in Fig.14.

It can be seen that the present unsteadiness is gradually damped in time which suggests that the flow tends to a steady state. In the experiment only the pressure amplitude (Δp) was recorded for this case, whereas the time period (T) was not. The amplitude of the first computational cycle is already underestimated by the numerical method, as can be seen from Table 2. Figs.15, 16, showing the two extreme shock envelopes

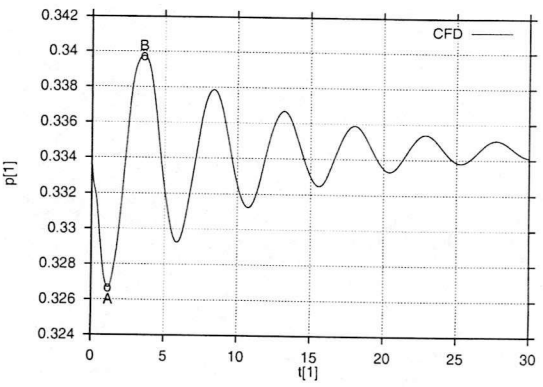

Figure 14: Mach 2.21 spiked 50^o cone: pressure history at the probe point

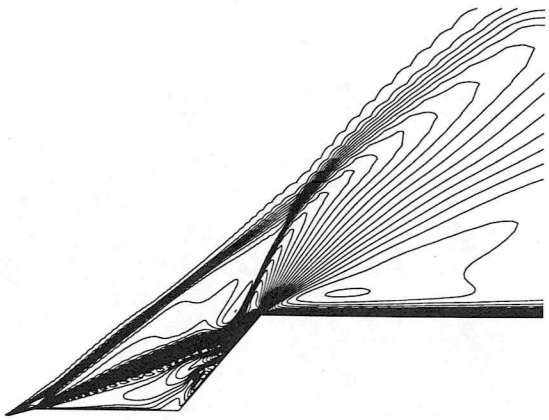

Figure 15: Mach 2.21 spiked 50^o cone: Mach contours corresponding to point A

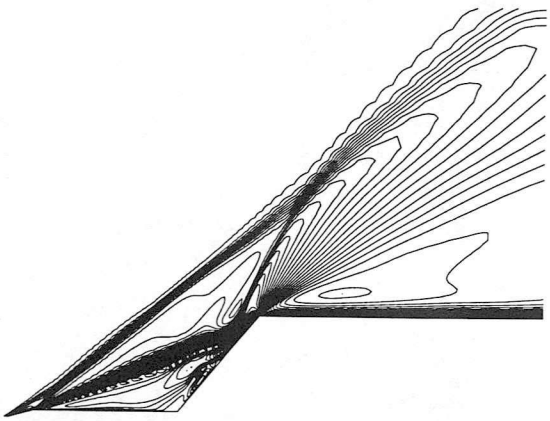

Figure 16: Mach 2.21 spiked 50^o cone: Mach contours corresponding to point B

corresponding to points A and B in the pressure history, are provided for information only, and indeed no significant difference is visible from them. Therefore, this case is not suitable for description or explanation of the flow mechanism.

	Experiment	Calculation
Δp [1]	0.05	0.013
T [1]	-	5.0

Table 2: Mach 2.21 spiked 50^o cone: Comparison with the experiment

It has to be added, that the experiment identified a definitive oscillation at the supersonic freestream for the 70^o half-cone angle case only. Despite that pressure amplitude was recorded in some other cases as well (such as this one), but because of the very small value of amplitude and the not observable difference in the Schlieren photographs they were not classified as oscillation.Therefore the computational results are in agreement with the experiment, as they predict a small oscillation tending to a stable state.

5.2 Spiked 50^o Cone at Mach 6.00

The oscillation mode in this case was more pronounced than above, with clearly developed and repeating cycles present in the pressure history at the probe point (see Fig.17). The steady state was reached by using 1000/0.4 explicit and 200/10 implicit steps before starting the unsteady part, which had the parameters of $\Delta t = 0.05$ for the real time step, 5 for the implicit CFL and t_{final}=40 for the final time.

Unfortunately, there was no experimental pressure history available to compare the shapes of the graphs, but the value of the pressure amplitude (Δp) and the time period (T) were recorded. The comparison is given in Table 3 which shows an excellent agreement for the time period but a poorer one for the pressure amplitude.

	Experiment	Calculation
Δp [1]	0.046	0.019
T [1]	5.55	5.60

Table 3: Mach 6.00 spiked 50^o cone: Comparison with the experiment

The amplitude is again small and the two figures showing Mach number contours (Figs.18, 19), corresponding to the pressure extremes A and B on Fig.17 do not exhibit a clearly distinguishable difference.

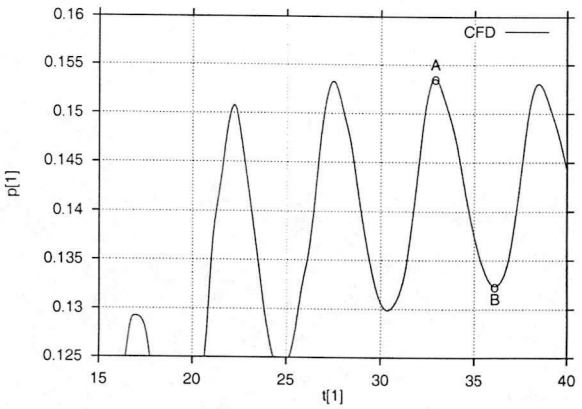

Figure 17: Mach 6.00 spiked 50^o cone: pressure history at the probe point

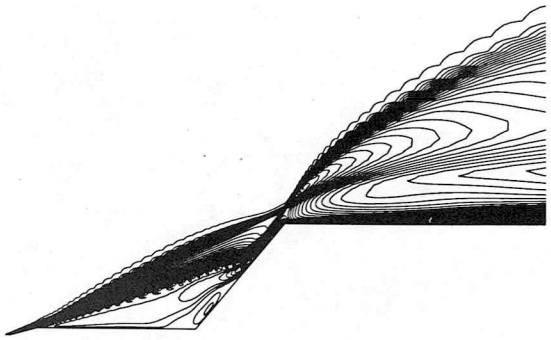

Figure 18: Mach 6.00 spiked 50^o cone: Mach contours corresponding to point A

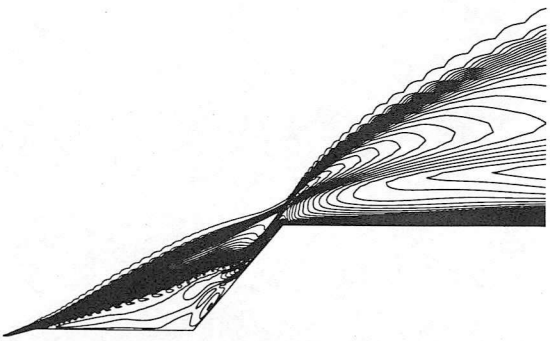

Figure 19: Mach 6.00 spiked 50^o cone: Mach contours corresponding to point B

5.3 Spiked 70° Cone at Mach 2.21

In the experiments of [18], at a freestream Mach number of 2.21 oscillation was obtained for the 70° half-angle cone only and for a limited range of $0.8 < l/D < 1.05$. In contrast, oscillation at Mach 6.00 was observed for all the half-cone angles between 50° to 90° for ranges of l/D typically of the order of 1.

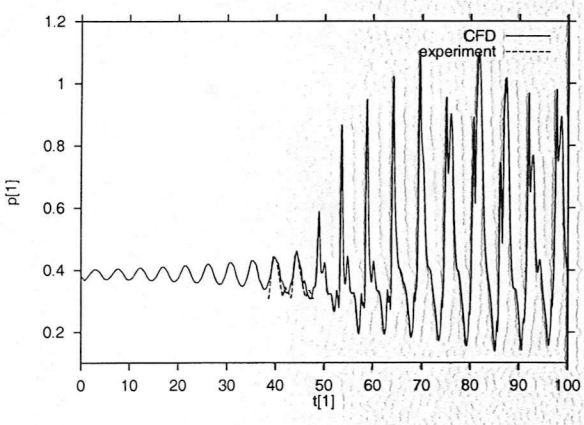

Figure 20: Mach 2.21 spiked 70° cone: full pressure history at the probe point

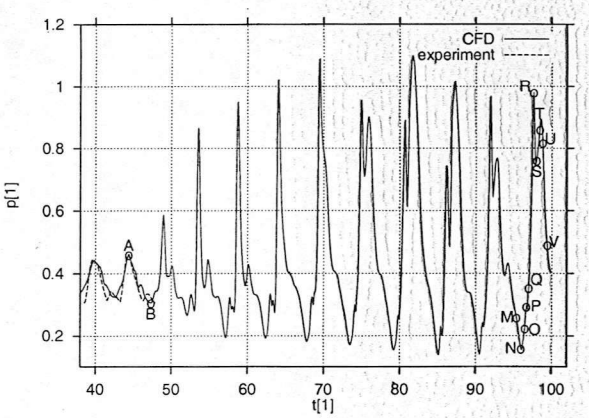

Figure 21: Mach 2.21 spiked 70° cone: detailed pressure history at the probe point

To obtain an initial steady state, 2000/0.4+400/10 steps were used, while the unsteady part of the calculation advanced with the real time step of 0.05 and implicit CFL of 10. However, as mentioned in section 4.1, this particular case showed a very interesting feature of a transient phase before developing the pulsation mode on the medium grid for an extended run, and therefore a very large, $t_{final} = 100$ value was used for the final real time.

The full pressure history at the probe point is shown in Fig. 20. The first ten cycles are gradually strengthened in time until reaching the pressure amplitude and time period comparable with the ones identified as oscillation in the experiment (shown by dashed line in Fig. 21 and Table 4). However, at around t=50 they instantly change to a rather different type of unsteadiness manifested by an order of magnitude larger pressure amplitude and a very much different cycle shape than before.

		Experiment	Calculation
oscillation cycle	Δp [1]	0.144	0.153
	T [1]	4.57	4.55
pulsation cycle	Δp [1]	1.04*	0.82
	T [1]	5.26*	5.45

Table 4: M2.21 Spiked 70° Cone: Comparison with the experiment (* values correspond to l/D=0.8)

Flow visualisation of a cycle from both these parts of the pressure history is shown in Figs.22,23 (corres-

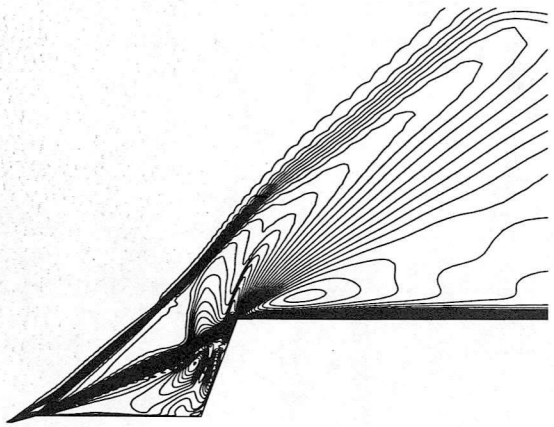

Figure 22: Mach 2.21 spiked 70° cone: Mach contours for point A

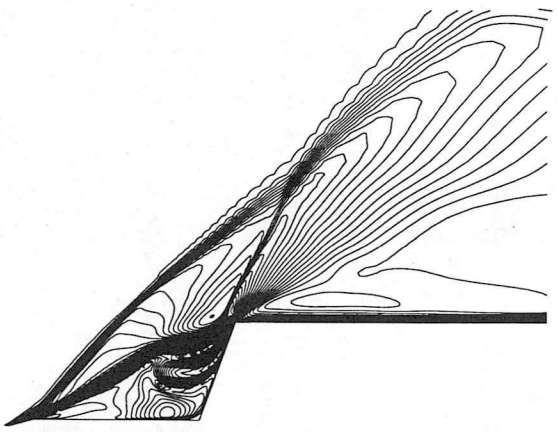

Figure 23: Mach 2.21 spiked 70° cone, Mach contours for point B

ponding to points A and B in the more detailed pressure history, Fig.21) and Figs.25- 34 (corresponding to points M-V in Fig.21). It is apparent from these shock envelopes, that while the first two figures might be representative of oscillation with a foreshock inflection travelling downstream and then initiating again at the spike tip in the next cycle, then the later ones correspond to pulsation, with an expanding and collapsing blunt body bow shock.

The explanation of the phenomenon, that two distinct modes are present at the same geometry could lie in the fact, that, as mentioned before, the l/D=0.9 spike length is very close to the measured boundary, where oscillation should change to pulsation (at around 0.8 in Fig.24 taken from the experimental data of [18]). However, while in the experiment the spike length was gradually decreased in time and therefore affected by the previous flow conditions, the flow was derived directly from the freestream conditions in our case, with no prior information about the flow before. It was observed in the experiment, that the oscillation/pulsation boundary occurred at 10-15% higher l/D, when the spike length was approached from the other direction (i.e. increased). This corresponds exactly to the calculated l/D=0.9 case, in which the pressure amplitude of the last computational cycle could be said to agree well with the one corresponding to l/D=0.8 in Fig.24, see Table 4.

Note that the fine grid pressure history of this case (shown earlier in section 4.1) yields an even better matching of the amplitudes: experiment recorded Δp= 1.04 at l/D=0.8, while CFD also predicts Δp=1.04 (read from Fig.7) at l/D=0.9. It should be emphasized again, that despite the better agreement from the fine grid calculation the medium grid was chosen because of its less costly computation but still reasonable prediction.

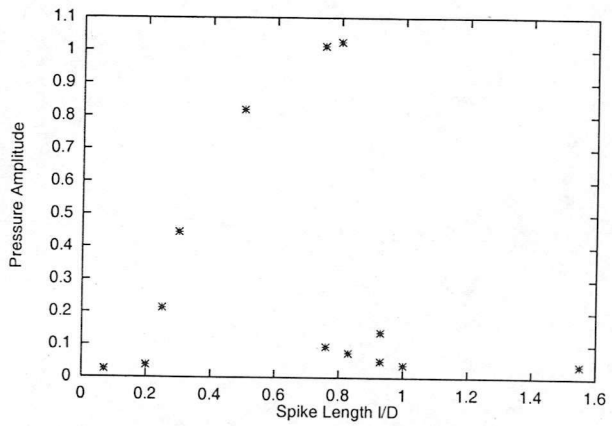

Figure 24: Mach 2.21 spiked 70^o cone: experimental pressure amplitudes for various spike lengths (Ref. [18])

A detailed description of the oscillation and pulstion modes is given here. Starting with oscillation, Figs.22 and 23 showing the two extreme shock envelopes display a major difference in the shapes of the foreshock and the shear layer. In Fig.22, corresponding to a pressure maximum, both the foreshock and the shear-layer lie on an almost straight line. On the other hand, Fig.23, corresponding to the pressure minimum (point B) on the pressure history, shows a convex foreshock and a curved shear-layer reattaching to the body shoulder at a higher angle relative to the cone face. Also note the location of the separation point; while it is in the rearmost position in Fig.22, then its movement toward the spike tip causes the appearance of the foreshock inflection at the spike tip initially, and which then moves rearward (Fig.23),toward the cone-shoulder. The inflection also causes the foreshock-aftershock intersection to occur more downstream than

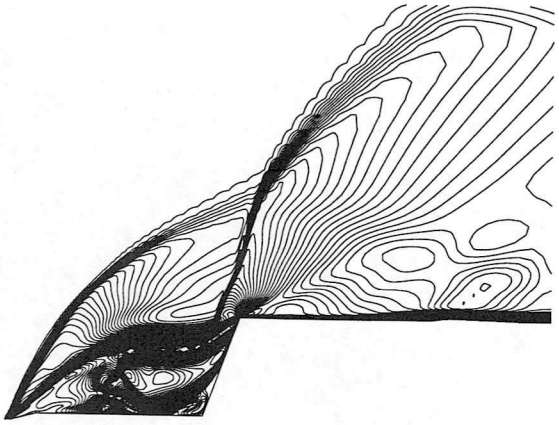

Figure 25: Mach 2.21 spiked 70^o cone, Mach contours for point M

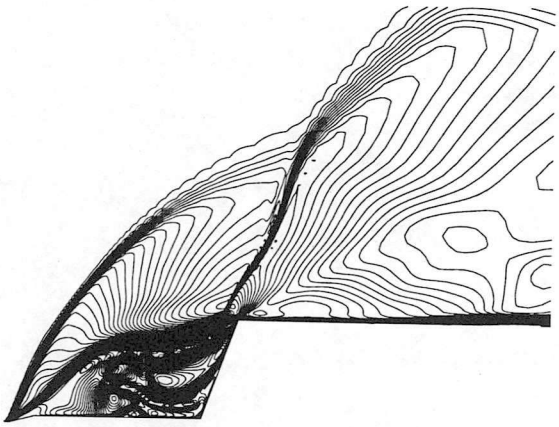

Figure 26: Mach 2.21 spiked 70^o cone, Mach contours for point N

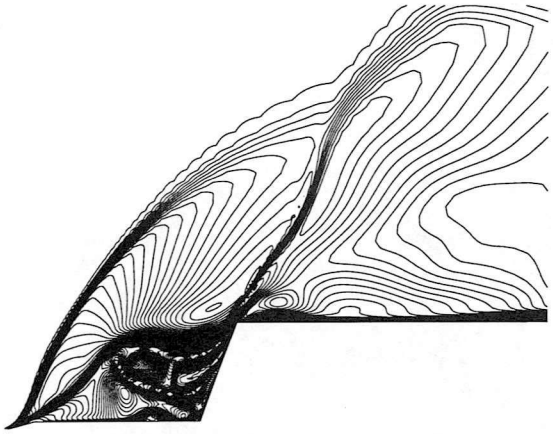

Figure 27: Mach 2.21 spiked 70^o cone, Mach contours for point O

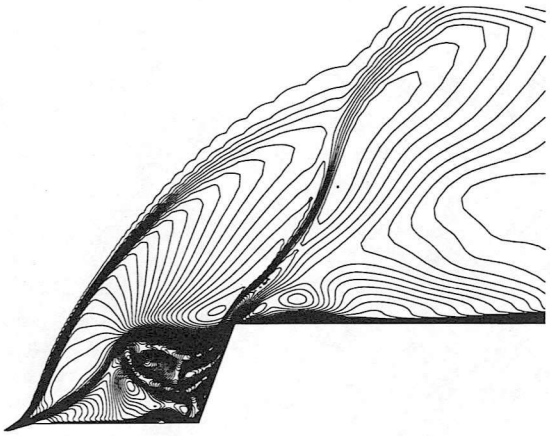

Figure 28: Mach 2.21 spiked 70^o cone, Mach contours for point P

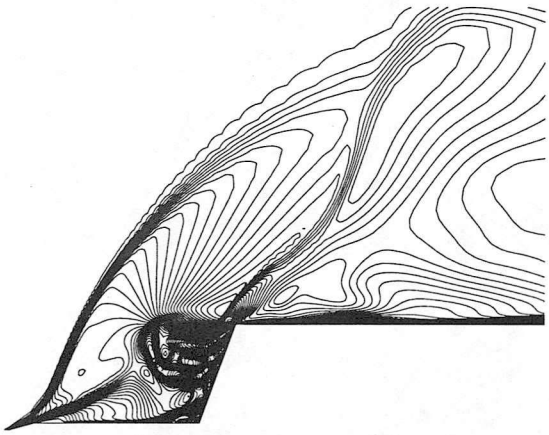

Figure 29: Mach 2.21 spiked 70^o cone, Mach contours for point Q

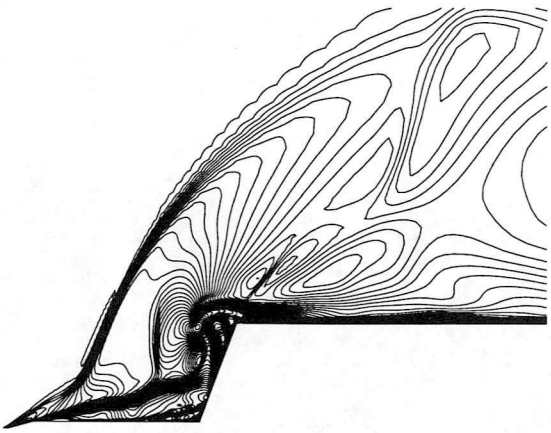

Figure 30: Mach 2.21 spiked 70^o cone, Mach contours for point R

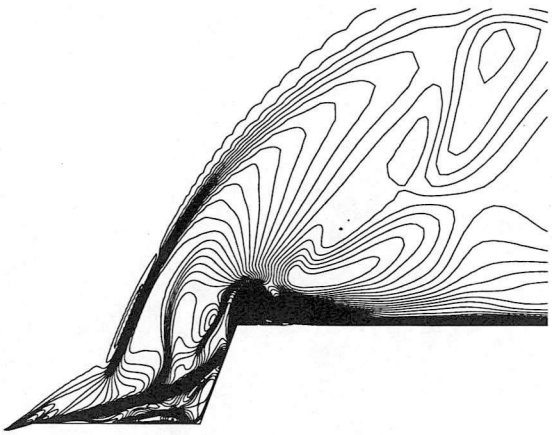

Figure 31: Mach 2.21 spiked 70^o cone, Mach contours for point S

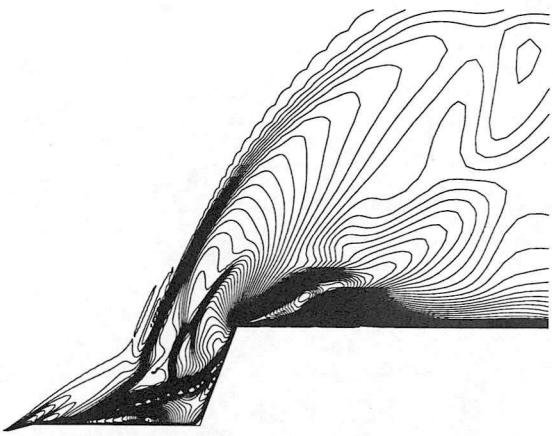

Figure 32: Mach 2.21 spiked 70^o cone, Mach contours for point T

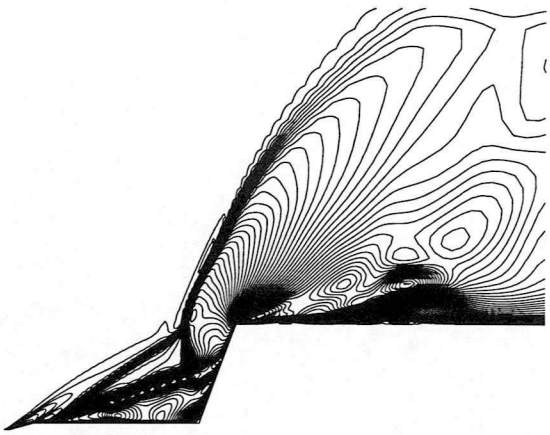

Figure 33: Mach 2.21 spiked 70^o cone, Mach contours for point U

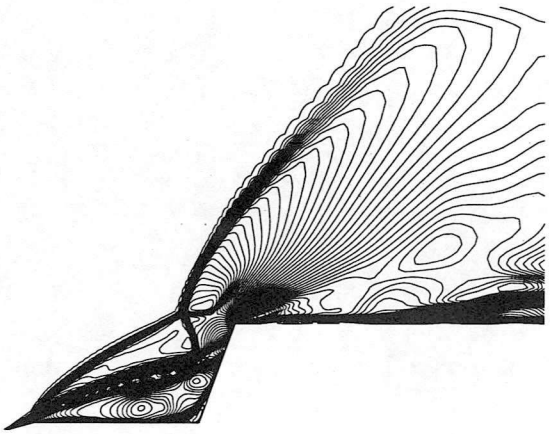

Figure 34: Mach 2.21 spiked 70^o cone, Mach contours for point V

in Fig.22.

On the other hand, the pulsation cycle manifests rather different flow features. Starting with Fig.25 the expanded foreshock has nearly completed the decompression. As the foreshock starts its excursion toward the cone face, the shear layer collapses and a boundary layer separation takes place at the spike root, which then moves toward the spike tip (Figs. 26-29). In Fig.30, which corresponds to the maximum pressure on the cone face, the first sign of the creation of a new bow wave is visible, as though the cone was impulsively accelerated to supersonic speed by the collapsing shock approaching the cone face. In the same time instant, the separation point has reached the spike half-length. The new bow wave's growth is seen in Fig. 31, 32, until it merges with the collpasing bow wave at the freestream shock detachment distance (Fig. 33). In the same figure the separation point has reached the spike tip shoulder and as it moves further forward to the spike tip, the new foreshock starts to expand laterally (Fig.34).

5.4 Spiked 70^o Cone at Mach 6.00

This case needed special attention for the choice of the unsteady parameters. In contrast to the supersonic case, no implicit steps could be used here for reaching the starting solution because of the obviously larger deviation of the cell values throughout the computational domain in the hypersonic freestream. Therefore 1000/0.4 explicit steps were used to obtain an initial state for the unsteady calculation, which then advanced with a real time step of 0.005 and a CFL number of 5 up to the final real time of 30.

	Experiment	Calculation
Δp [1]	0.134	0.344
T [1]	5.31	5.07

Table 5: Mach 6.00 spiked 70^o cone: Comparison with the experiment

In Fig.35 experimental and computational pressure histories at the pressure tap are shown. Table 5 shows the numerical comparison of the results; the pressure amplitude is overestimated, while the time periods are in excellent agreement. However, two graphs share the same trends and therefore it is assumed that qualitatively the same flow sequence takes place as in the experiment. This is described in the following, using a typical cycle from the pressure history, marked with-letters A-J. This description agrees well with the one given in [18].

Beginning with Fig.36 the cycle is approximately midway through its decompression and as the separation is emanating from the spike tip, it could be termed

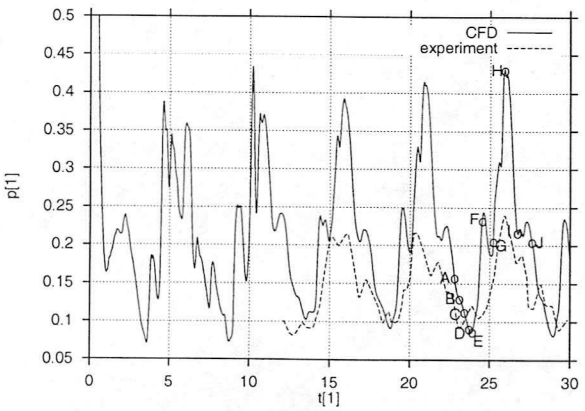

Figure 35: Mach 6.00 spiked 70^o cone: pressure history at the probe point

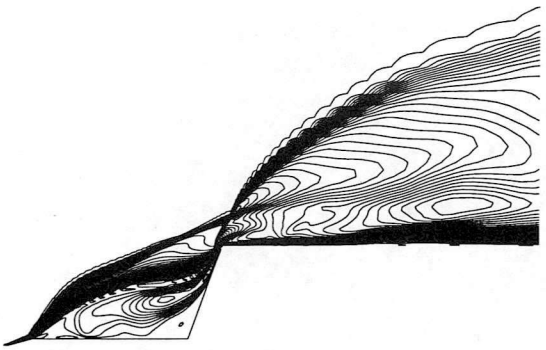

Figure 36: Mach 6.00 spiked 70^o cone , Mach contours for point A

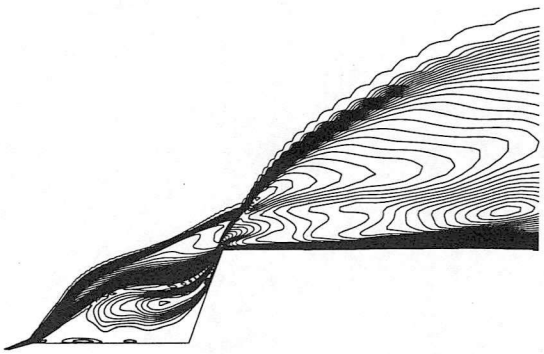

Figure 37: Mach 6.00 spiked 70^o cone, Mach contours for point B

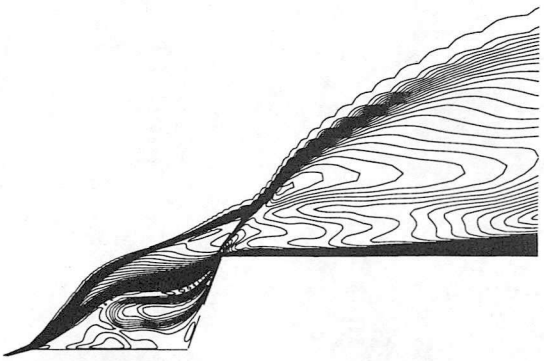

Figure 38: Mach 6.00 spiked 70^o cone, Mach contours for point C

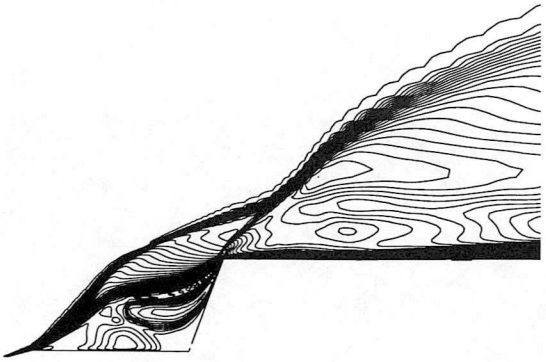

Figure 39: Mach 6.00 spiked 70^o cone, Mach contours for point D

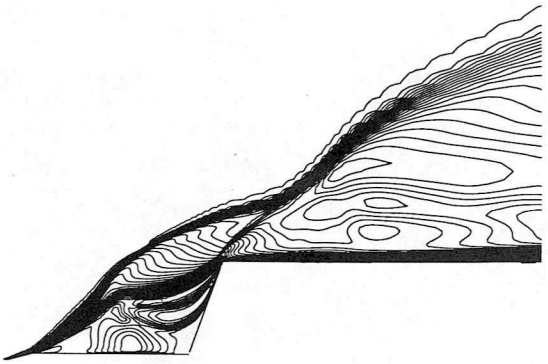

Figure 40: Mach 6.00 spiked 70^o cone, Mach contours for point E

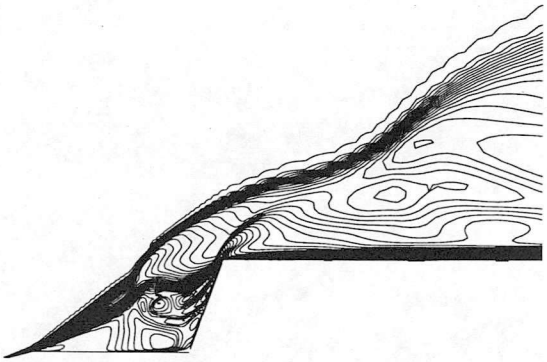

Figure 41: Mach 6.00 spiked 70^o cone, Mach contours for point F

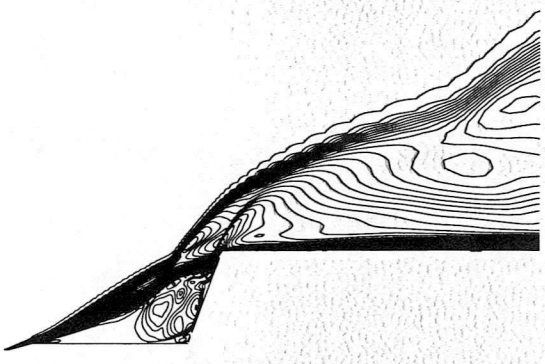

Figure 42: Mach 6.00 spiked 70^o cone, Mach contours for point G

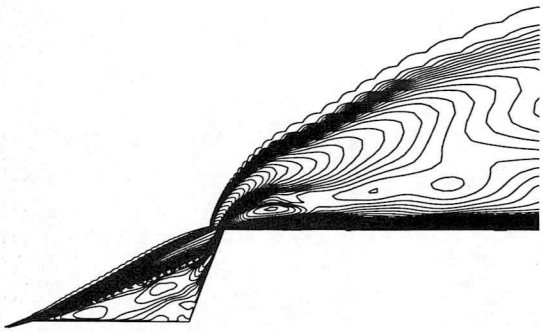

Figure 44: Mach 6.00 spiked 70^o cone, Mach contours for point I

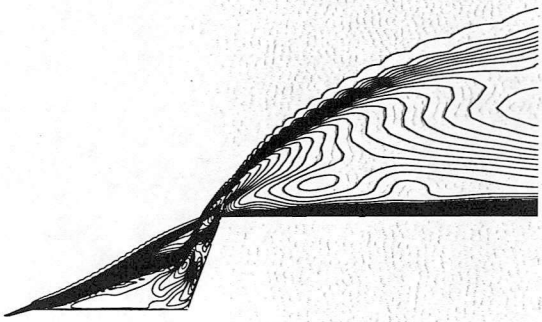

Figure 43: Mach 6.00 spiked 70^o cone, Mach contours for point H

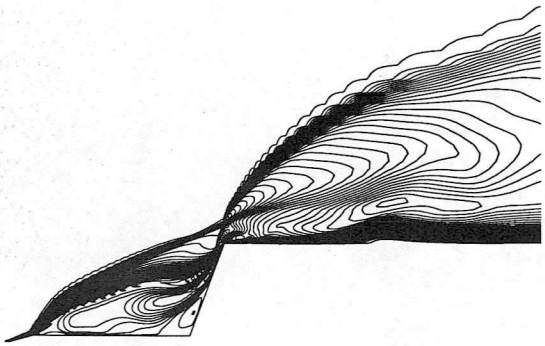

Figure 45: Mach 6.00 spiked 70^o cone, Mach contours for point J

as leading edge type. Figures 36-40 show the foreshock changing inflection as the pressure attains its minimum value. The inflection change begins at the tip and moves rearward.In Fig.40 at the minimum pressure, the shear layer is a clearly kinked line, which creates a large angle of the shear layer relative to the cone face at the shoulder. From Fig.41 to 43 the separation point moves away from the tip as the pressure goes from its minimum to maximum value. Note, that the maximum pressure coincides with the rearmost position of separation and also the steepest shear layer angle at reattachment. The separation point then reverses its direction, which causes the shear layer shape - and therefore its angle at the reattachment as well - to change back from convex to concave. By Fig.43 its form is nearly a straight line, and on Fig.45 the separation point has once again reached the spike tip.

5.5 Spiked Cylinder at Mach 2.21

The calculation was carried out in the same way as the spiked 70^o cone at Mach 2.21, apart from the value of the final real time, which is set at 33. The pressure histories predicted by CFD and from the experiment are shown in Fig.46 and in Table 6.

	Experiment	Calculation
Δp [1]	1.23	1.00
T [1]	5.71	5.59

Table 6: Mach 2.21 spiked cylinder: Comparison with the experiment

As can be seen, the dominant pressure amplitude is slightly underestimated by the numerical method but the time periods again agree well. The shapes of the graphs also show an excellent similarity, which allows

one to suppose that the processes taking place in the flow are predicted qualitatively.

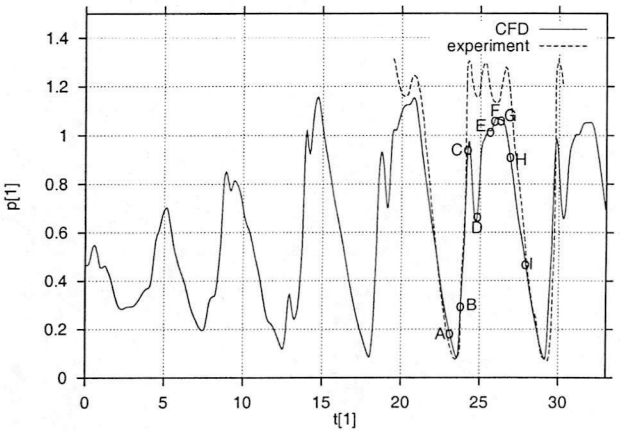

Figure 46: Mach 2.21 spiked cylinder: pressure history at the probe point

Following [18] a typical cycle was chosen from the history, marked with letters A-I, corresponding to Mach contour plots shown in Figs.47-59. In Fig.47 the expanded foreshock is to be seen as the decompression has been nearly completed. As the collapsing shock begins its migration toward the cylinder face, a compression shock wave is being created at the face as though the cylinder was impulsively accelerated to supersonic speed.The first evidence of its formation could be seen on Fig.48, and the growth of this new bow wave is visible on Fig.50. By Fig.51 the new bow shock is fully formed and separates the spike boundary layer. This separation is clear from the vector plots (Figs.49,52).The collapsing bow wave continues toward the cylinder face until it merges with the new bow wave at the free stream shock detachment distance. The separation point continues toward the spike tip (see the vector plots on Figs.55, 57), but the pressure at the model face does not decrease. This is due to the relatively long time required for the separation point to reach the spike tip and results in a column of highly disturbed flow (Figs.53,54,56) impacting on the cylinder face and causing a pressure plateau. In Fig.56 the end of this pressure plateau is reached and the foreshock begins expanding. Formation of an oblique shock can be observed on the body downstream on the face. This is caused by the recompression of the flow as it is overexpanded coming from the region of the face showing that there is a mass flux out of the foreshock region. The process of the expansion of the foreshock is shown in Fig.58 and Fig.59. The pressure decreases throughout this portion of the cycle.

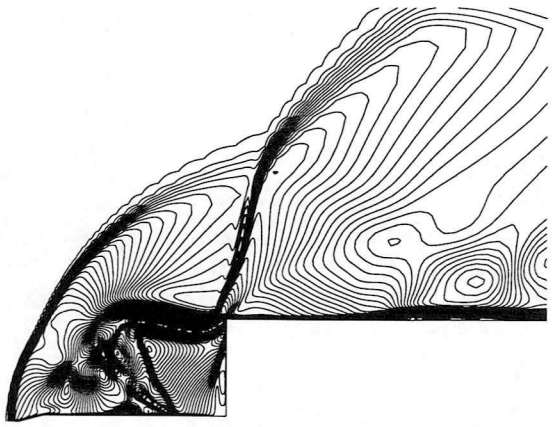

Figure 47: Mach 2.21 spiked cylinder: Mach contours, point A

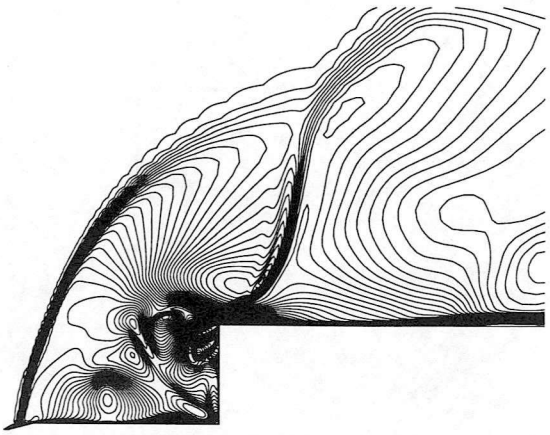

Figure 48: Mach 2.21 spiked cylinder: Mach contours, point B

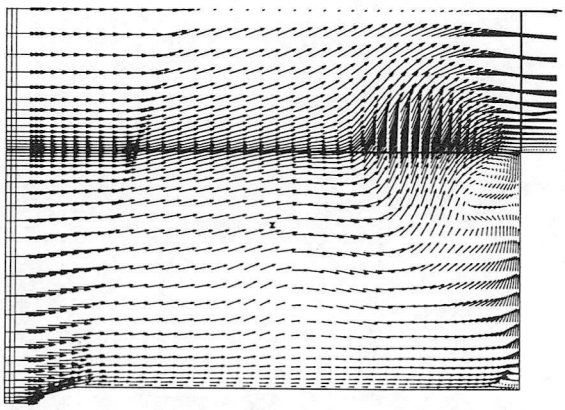

Figure 49: Mach 2.21 spiked cylinder: vector plots, point B

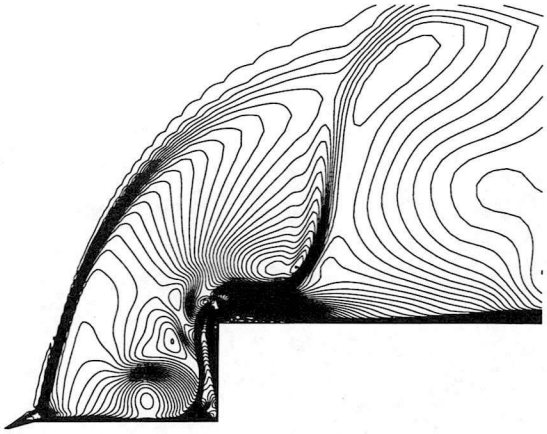

Figure 50: Mach 2.21 spiked cylinder: Mach contours, point C

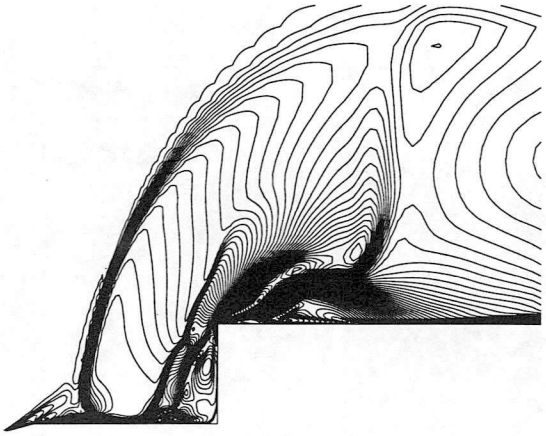

Figure 51: Mach 2.21 spiked cylinder: Mach contours, point D

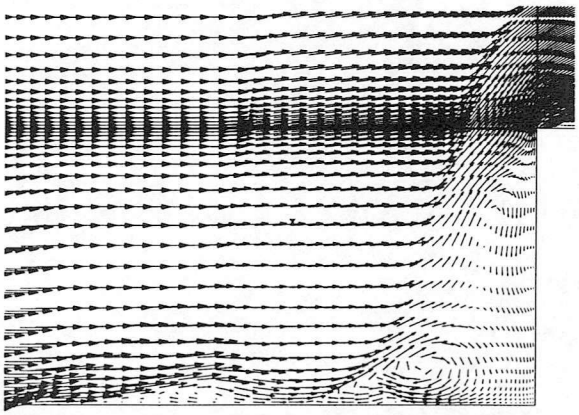

Figure 52: Mach 2.21 spiked cylinder: vector plots, point D

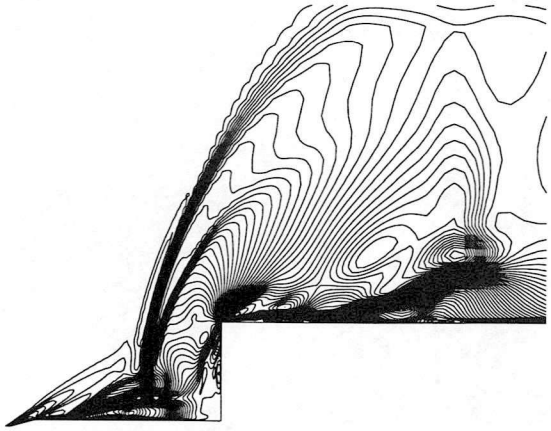

Figure 53: Mach 2.21 spiked cylinder: Mach contours, point E

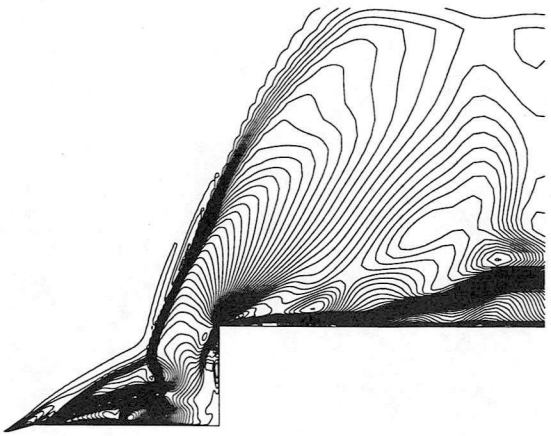

Figure 54: Mach 2.21 spiked cylinder: Mach contours, point F

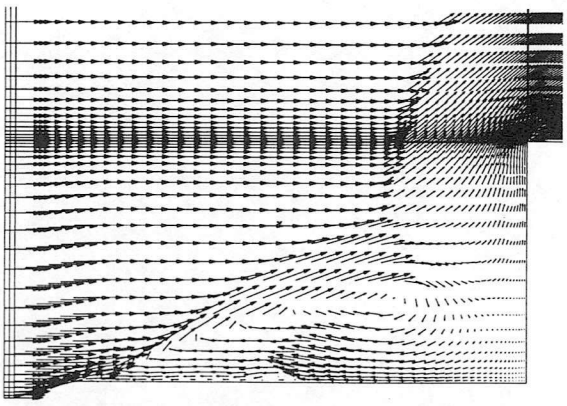

Figure 55: Mach 2.21 spiked cylinder: vector plots, point F

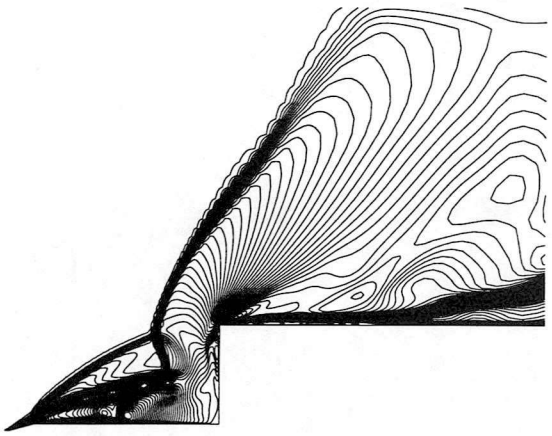

Figure 56: Mach 2.21 spiked cylinder: Mach contours, point G

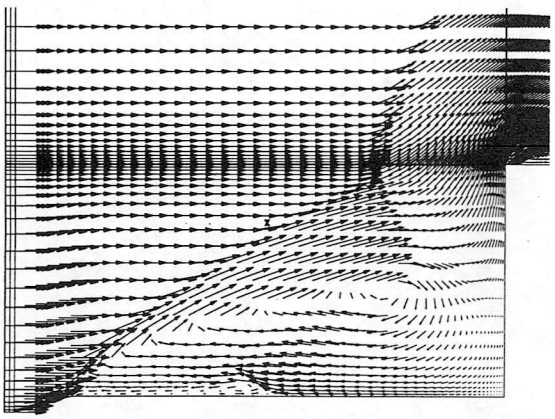

Figure 57: Mach 2.21 spiked cylinder: vector plots, point G

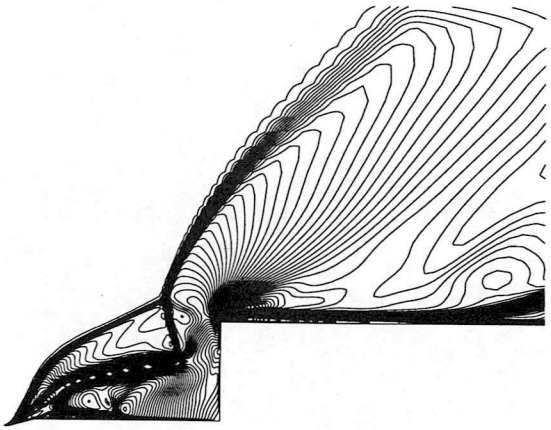

Figure 58: Mach 2.21 spiked cylinder: Mach contours, point H

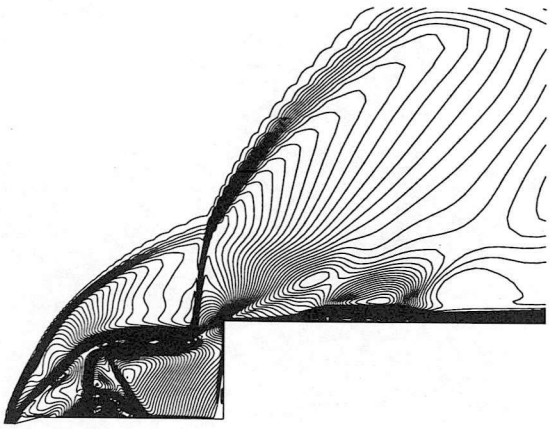

Figure 59: Mach 2.21 spiked cylinder: Mach contours, point I

5.6 Spiked Cylinder at Mach 6.00

The calculation of this case again needed careful choice of the parameters similar to the Mach 6.00 spiked 70° cone (see section 4.4). However, the maximum allowable real time step and the implicit CFL was even less i.e. Δt=0.004 and CFL=4.0.

The history of the computed and experimental pressure monitored at the probe point is shown in Fig.60 and compared in Table 7. The pressure amplitudes are overestimated by the numerical method, but the qualitative behaviour is generally correct.

Similar to the above cases, a typical cycle (marked with letters A-J) was chosen to introduce the processes of the pulsation arising in hypersonic freestream. In Fig.61 the decompression has nearly been completed as the shock then begins its migration towards the model face. As it passes the quarter spike position, the minimum pressure is recorded at the face (see Fig.62).

	Experiment	Calculation
Δp [1]	1.21	1.70
T [1]	5.93	5.96

Table 7: Mach 6.00 spiked cylinder: Comparison with the experiment

Note that in the supersonic case this pressure reversal was obtained much earlier when the collapsing shock passed the spike tip (see Fig.47,48). During the same portion of the cycle a compression/shock wave is being created at the face (Fig.63) as though the blunt body was being impulsively accelerated to supersonic speed. This wave in turn separates the spike boundary layer (Fig.64) as for the supersonic case. The separation point then moves very rapidly towards the spike

tip as the collapsing bow wave continues toward the face. In Fig.65 the two waves have merged and the separation point has very nearly reached the spike tip.

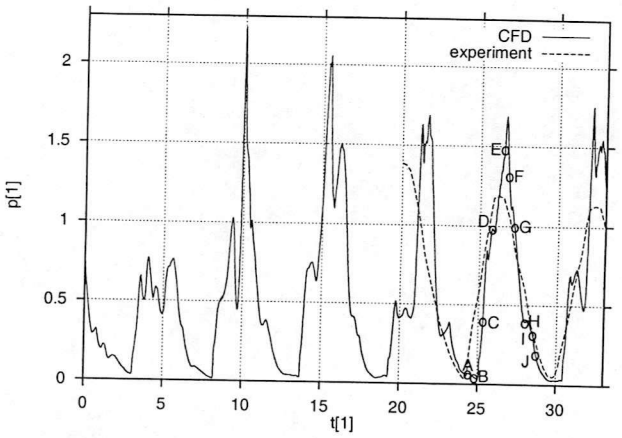

Figure 60: Mach 6.00 spiked cylinder: pressure history at the probe point

The maximum pressure has also been recorded at this point of the cycle. In Fig.66, the separation point has reached the tip of the spike. Then the oblique conical foreshock begins to expand laterally, as the pressure rapidly decreases. This causes the shock-shock intersection to move towards the shoulder of the cylinder (Fig. 67,68,69). It can be observed in Fig.69, that the inertia of the expanding foreshock is able even to detach this shock from the spike tip and to create another bow shock in front of the spike. This feature of the flow was not picked up by the experiment, probably because of the extremely short time of its existence and that it does not take place in every cycle (which is true even in the computation).

In Fig.70, the expanding foreshock-bowshock intersection has been displaced beyond the shoulder, and the original bow wave is being washed downstream. The foreshock continues its expansion as the pressure continues to decrease and reaches the characteristics at the start of the cycle (point A).

As one can observe, there are two major differences between the supersonic and hypersonic case. First is the missing pressure plateau in the Mach 6.00 case. This is caused by the much faster movement of the separation point towards the spike tip, which leaves no time for the creation of the turbulent column of the flow apparent in the supersonic case. In the hypersonic case, therefore, this feature is by-passed. The second main difference is in the place where the collapsing and the new bow wave merge. While in the supersonic case it happened at the free-stream shock-detachment distance, it happens much closer to the cylinder in the hypersonic case where there is no time for the new bow shock to reach the freestream shock stand off distance.

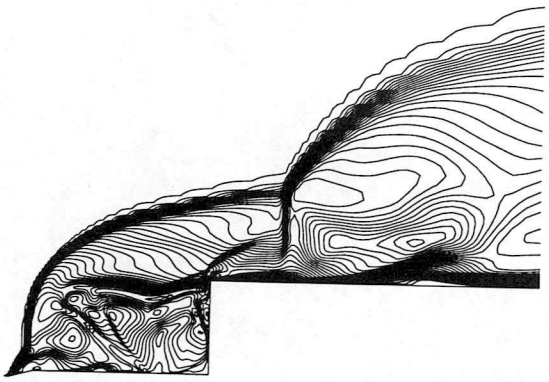

Figure 61: Mach 6.00 spiked cylinder: Mach contours, point A

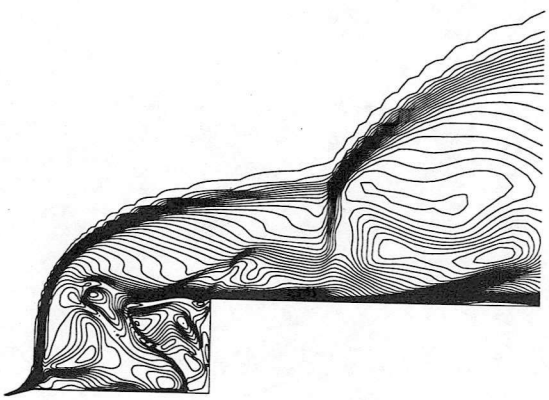

Figure 62: Mach 6.00 spiked cylinder: Mach contours, point B

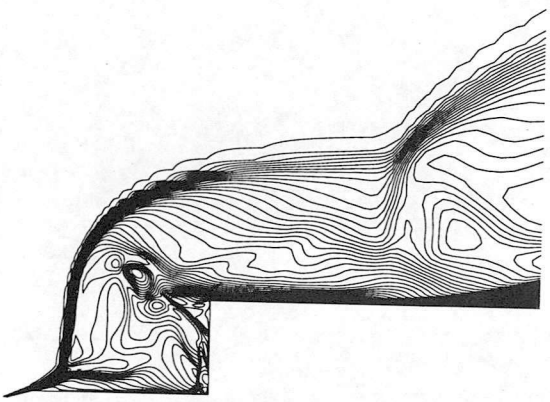

Figure 63: Mach 6.00 spiked cylinder: Mach contours, point C

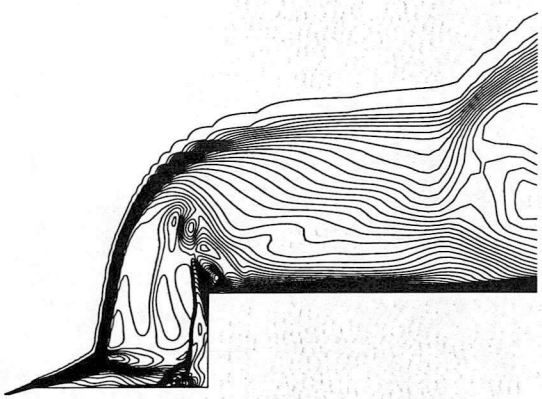

Figure 64: Mach 6.00 spiked cylinder: Mach contours, point D

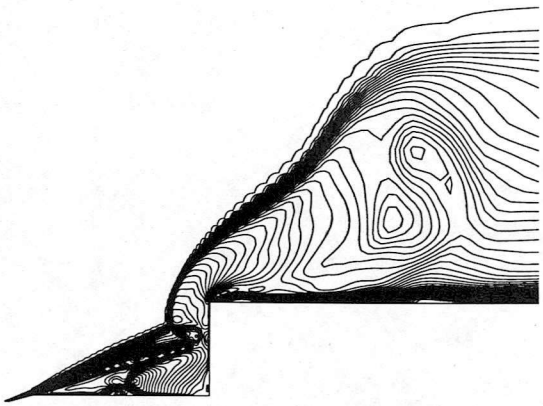

Figure 67: Mach 6.00 spiked cylinder: Mach contours, point G

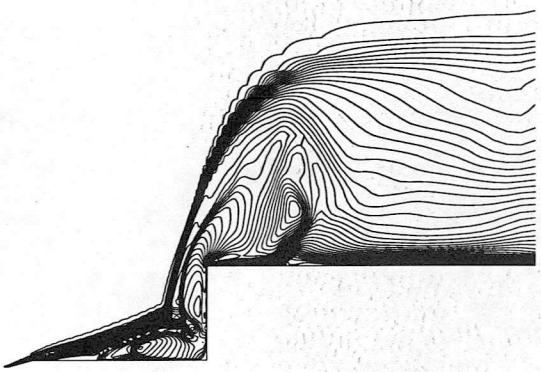

Figure 65: Mach 6.00 spiked cylinder: Mach contours, point E

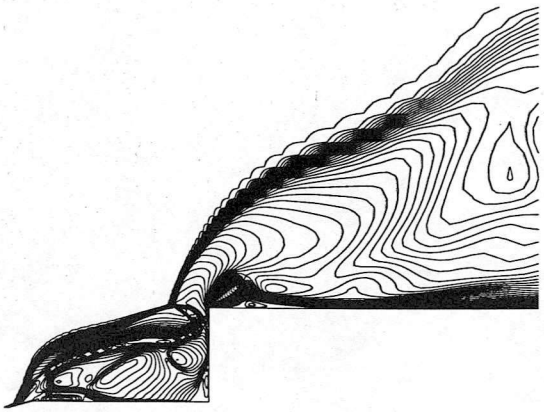

Figure 68: Mach 6.00 spiked cylinder: Mach contours, point H

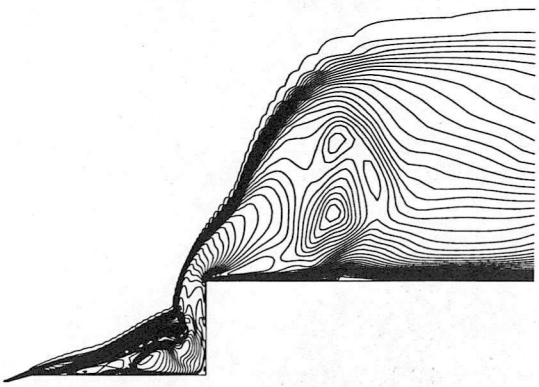

Figure 66: Mach 6.00 spiked cylinder: Mach contours, point F

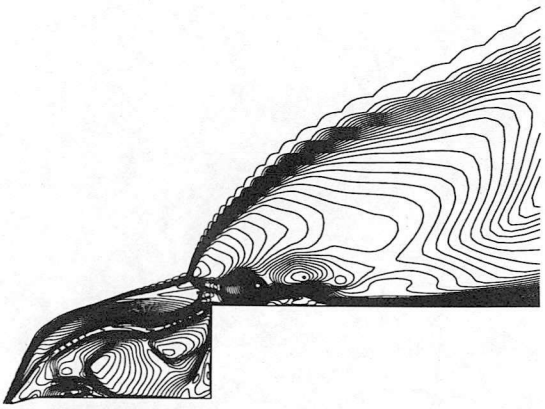

Figure 69: Mach 6.00 spiked cylinder: Mach contours, point I

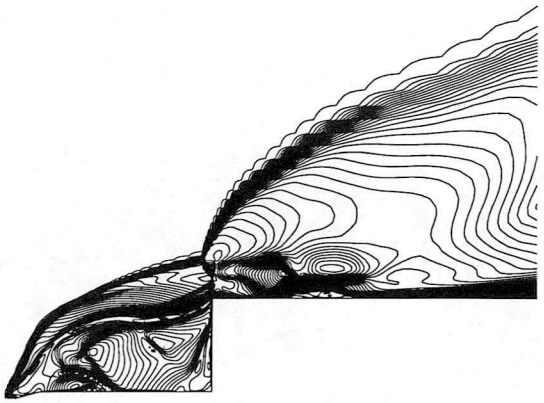

Figure 70: Mach 6.00 spiked cylinder: Mach contours, point J

The above results agree well with the experiment apart from the timing of the pressure extremes. In the experiment the minimum pressure is recorded when the collapsing shock passes the half spike length, whereas computation predicts this to happen slightly earlier, approximately at the quarter spike length. Also, the experiment reports the pressure maximum at the time instant when the separation point reaches the spike tip, while the computational results show this to happen earlier. However, as the above processes take place very rapidly (pulsation frequency is around 7600 Hz), the deviations in timing could be explained by errors due to the complexity of synchronisation in the experiment.

6 Comparison of the Mach 6.00 Spiked Cylinder Visualisations with the Schlieren Shadowgraphs

The last phase of the validation consisted of a comparison of the numerically obtained shock envelopes with the experimental ones. The Mach 6.00 90^o case was chosen for this purpose, for which Schlieren shadowgraphs covering a whole cycle are available from [18].

However, because the very high frequency of the pulsation mode mentioned above, the limitations of the spark equipment meant that the photographic sequence could not be taken in one cycle and thus each of these shadowgraphs was obtained from a different cycle. The point timing of the photographs was recorded on the pressure history and using this information a typical cycle was constructed. These pictures are reproduced in Figs.72-74, 78-80 and 84-86.

On the other hand, the numerical method enabled visualisating all the frames within one particular cycle and as the cycles proved to be not repeatedly identical, slight differences between CFD and experiment are expected. As the Schlieren photographs depict the density gradients, density contours were chosen for visualisation the numerical results as well. These are shown in Figs. 75-77, 81-83 and 87-89.

Comparison of the above pictures shows that, in general, the numerically predicted shock envelopes are in excellent agreement with the experiment. The only exception could be Fig.75 where the strong bow shock in front of the cylinder has a rather curved shape, whereas it is a straight line in the Schlieren shadowgraph. Nevertheless, the main flow features, e.g. relative position of the collapsing and the new bow wave and the location of the separation point are well predicted in this figure as well.

Finally, the points corresponding to the above density contours were found on the pressure history, as shown in Fig.71.

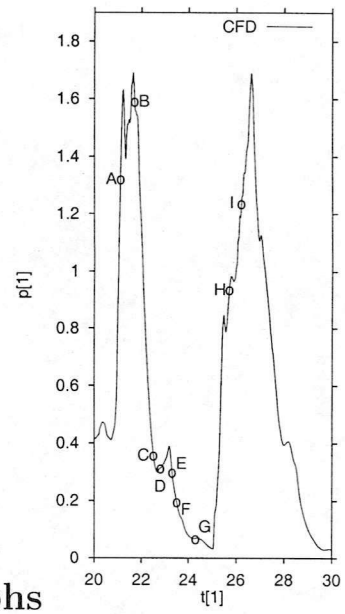

Figure 71: Numerically obtained pressure history at the probe point for the spiked 90^o case, l/D=1.0, M=6.00

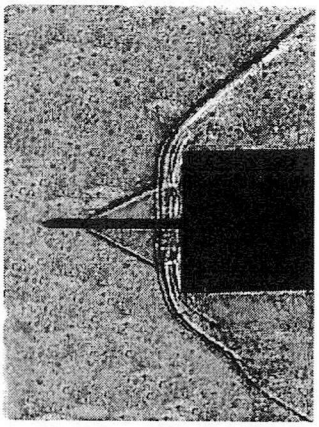

Figure 72: Schlieren shadowgraph for point A (Ref.[18])

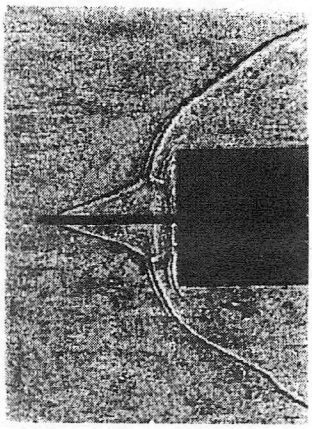

Figure 73: Schlieren shadowgraph for point B (Ref.[18])

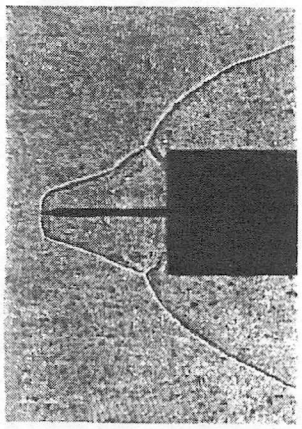

Figure 74: Schlieren shadowgraph for point C (Ref.[18])

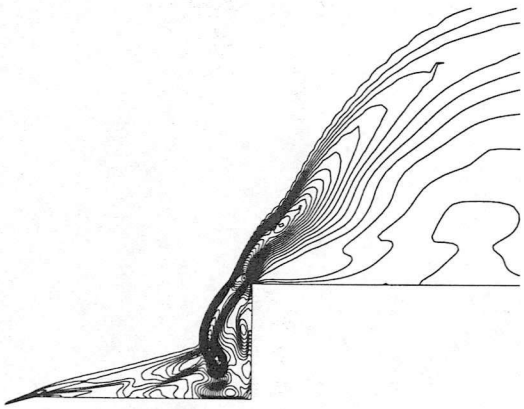

Figure 75: Computed density contours for point A

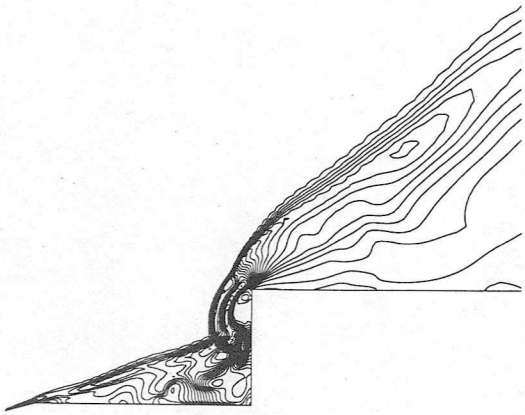

Figure 76: Computed density contours for point B

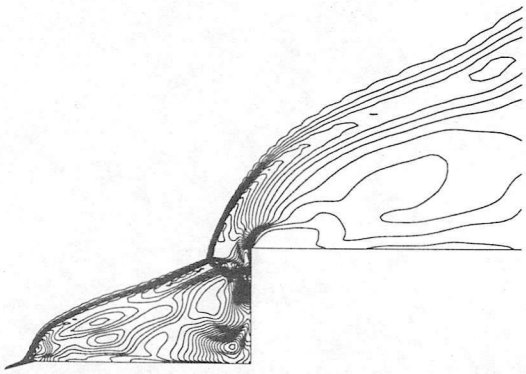

Figure 77: Computed density contours for point C

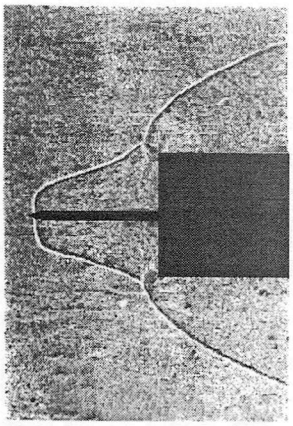

Figure 78: Schlieren shadowgraph for point D (Ref.[18])

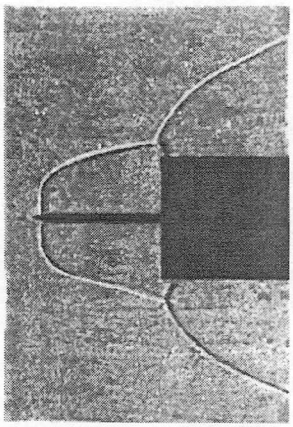

Figure 79: Schlieren shadowgraph for point E (Ref.[18])

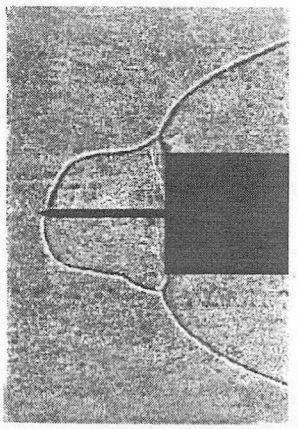

Figure 80: Schlieren shadowgraph for point F (Ref.[18])

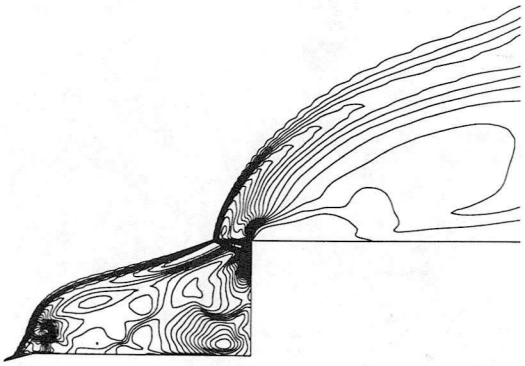

Figure 81: Computed density contours for point D

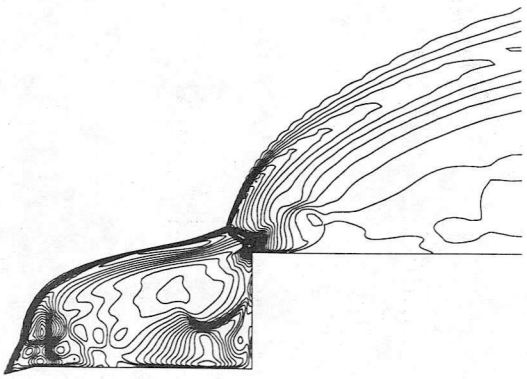

Figure 82: Computed density contours for point E

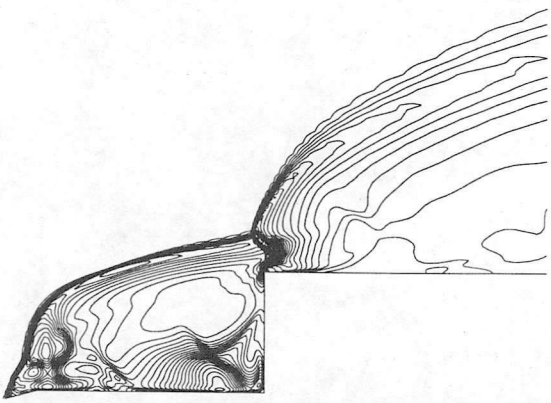

Figure 83: Computed density contours for point F

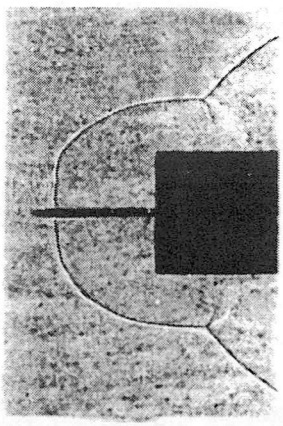

Figure 84: Schlieren shadowgraph for point G (Ref.[18])

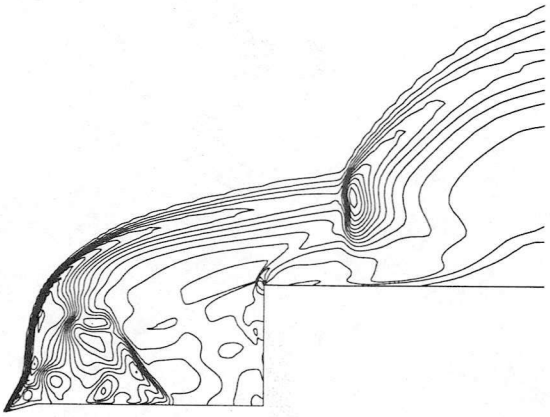

Figure 87: Computed density contours for point G

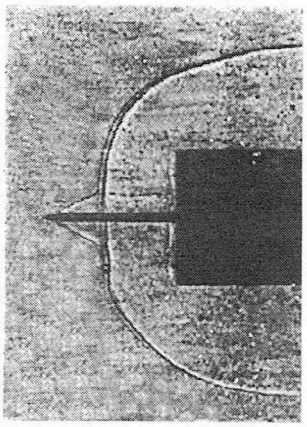

Figure 85: Schlieren shadowgraph for point H (Ref.[18])

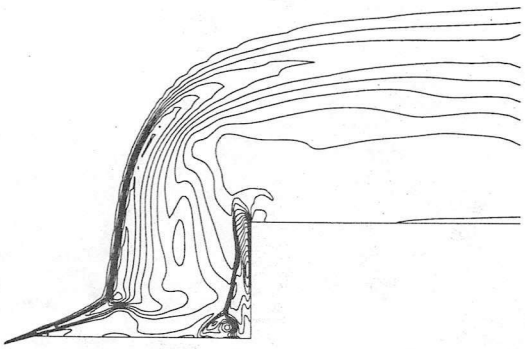

Figure 88: Computed density contours for point H

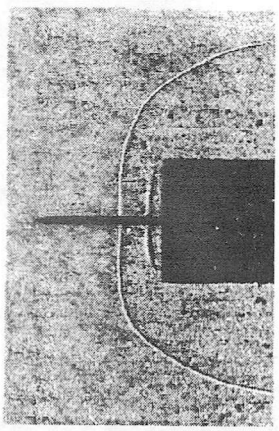

Figure 86: Schlieren shadowgraph for point I (Ref.[18])

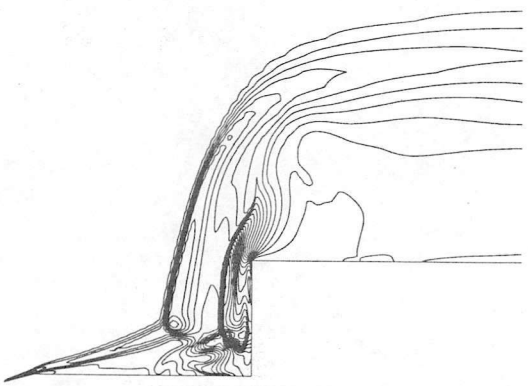

Figure 89: Computed density contours for point I

7 Conclusions and Future Work

The present paper documents some cases of numerical simulation of high-speed unsteady flows. Pressure histories at a particular pressure station were compared with the experiment.

It was found that there was no significant oscillation in the case of the spiked 50^o cone at Mach 2.21, while it was clearly developed for the Mach 6.00 case. In contrast to the experimentally recorded oscillation, the pulsation mode was predicted by the numerical method for the spiked 70^o cone at Mach 2.21. An explanation lies in this case being near the oscillation/pulsation boundary and hysteresis effects seen in the experiment. For the hypersonic case, oscillation was observed for the same configuration. The pulsation taking place in the supersonic/hypersonic spiked cylinder cases were also reproduced by the numerical method.

Qualitatively, the predictions are in general accord with experiment. Quantitative comparison of the results showed, that while predicted time periods were almost identical with the experiment, the computational pressure amplitudes were generally overpredicted.

Grid dependence tests showed that in the spiked 70^o cone cases the fine grid results in instant development of large amplitudes, while the medium grid may require some transient phase to properly develop the flow mode. Other cases showed less sensitivity to grid refinement or real time step size.

In addition, the activity of the proposed modifications to the numerical method for hypersonic flow (see section 3.2.) was monitored. In contrast to the steady flow calculations over the isolated body cases [24], where both of the modifications were essential in order to avoid the failure of the numerical method, the new entropy fix alone proved to be sufficient in the unsteady calculations, whereas the boundary condition modification was not active at all.

An interesting conclusion is, that despite CFD ensuring ideal conditions of modelling (perfect axisymmetry of the flow, no perturbations in the freestream) the cycles are not identically repeated. The same was observed in the experiment, but expected due to the "background noise" of the measurement. This suggests that these lack of cyclic behaviour are likely to be due to historical features in the flow behaviour.

Having demonstrated that the numerical method is correct, this allows detailed insight of any part of the flowfield enabled by CFD to be used in the future to investigate in detail the driving mechanisms of oscillation and pulsation.

An interesting feature of the flows over spiked bodies is the hysteresis effect in changing from stable flow to oscillation/pulsation when the spike length is gradually decreased or inreased in time. A future work shall tackle the numerical investigation of this phenomenon, which is a challenging problem requiring employment of time-dependent deforming of the computational grid in the unsteady code.

References

[1] Oswatitsch, K., "Der Druckrückgewinn bei Geschossen mit Rückstossantrieb bei hohen Überschallgeschwindigkeiten", *Bericht Nr 1005, Forch. & Entwickl. Heereswaffenamtes (Göttingen),* 1944. also NACA TM 1140

[2] Sterbentz, W.H., Evvard, J.C., "Criterions for Prediction and Control of Ram-Jet Flow Pulsations", *NACA TN 3506* 1955.

[3] Beastall, D., Turner, J., "The Effect of a Spike Protruding in front of a Bluff Body at Supersonic Speeds", *ARC R&M 3007* 1957.

[4] Eggers, A.J., Allen, M.J., "A Study of the Motion and Aerodynamic Heating of Ballistic Missiles Entering the Earth's Atmosphere at High Supersonic Speeds", *NACA TR 1281* 1958.

[5] Hunt, G.K., "Supersonic Wind Tunnel Study of Reducing the Drag of a Bluff Body at Incidence by means of a Spike", *RAE Report Aero 2606* 1958.

[6] Stalder, J.R., Nielsen, H.V., "Heat Transfer from a Hemisphere Cylinder Equipped with Flow Separation Spikes", *NACA TN 3792* 1954.

[7] Bogdonoff, S.M., Vas, I.E., "Preliminary Investigations of Spiked Bodies at Hypersonic Speeds", *Princeton University Report 412, 1958, also Journal of Aerospace Science, vol 26, No 2,* 1959.

[8] Crawford, D.H., "Investigation of the Flow over a Spiked-Nose Hemisphere-Cylinder at a Mach number of 6.8", *NASA TN D 118* 1959.

[9] Minges, M.L., "Ablation Phenomenology (a review)", *High Temperatures-High Pressures, Vol 1,* 1969.

[10] Kenworthy, M.A., Richards, B.E., "A Study of the Unsteady Flow over Concave Conic Models at Mach 15 and 20", *AFML TR 138* 1976.

[11] Abbett, M.J., Cooper, L., Dahm, T.J., Jackson, M.D., "Flow Characteristics about Concave Conic Forebodies at High Mach Numbers", *AIAA P 75-153,* 1975.

[12] Freeman, D.C.Jr., Talay, T.A., Austin, R.E., "Reusable Launch Vehicle Technology Program", *Acta Astronautica, Vol.41, No 11, pp 777-7902,* 1997.

[13] Jackson, J.E., Espenschied, E., Klop, J., "Control System for the X-33 Linear Aerospike Engine", *IEEE Aerospace Applications Conference Proceedings, Vol. 3, pp. 191-191,* 1998.

[14] Shoemaker, J.M., "Aerodynamic Spike Flowfields Computed to Select Optimum Configuration at Mach 2.5 with Experimental Validation", *AIAA Paper 90-0414,* 1990.

[15] Fujita, M., Kubota, H., "A Simulation of Flow Separation Effects Ahead of Blunt Bodies", *A Collection of Technical Papers, 4th International symposium of CFD, vol 1, University of California, Davis, CA, pp. 359-364* 1991.

[16] Mikhail, A.G., "Spike-Nosed Projectiles with Vortex Rings: Steady and Nonsteady Flow Simulations", *Journal of Spacecrafts and Rockets, vol 33, No 1, pp. 8-14,* 1995.

[17] Yamauchi, M., Fujii, K., Higashino, F., "Numerical Investigation of Supersonic Flows Around a Spiked Blunt Body", *Journal of Spacecraft and Rockets, vol 32, No 1, pp. 32-42,* 1995.

[18] Kenworthy, M.A., "A Study of Unstable Axisymmetric Separation in High Speed Flows", *PhD Thesis, Virginia Polytechnic Institute and State University,* March 1978.

[19] Badcock, K.J., Cantariti, F., Woodgate, M., Dubuc, L., and Richards, B.E., "Simulation of Unsteady Flows using the Pseudo Time Method", *Fourth ECCOMAS Computational Fluid Dynamics Conference, Athens, September 1998. Computational Fluid Dynamics '98. Ed. Papapillou, K.D., Tsahalis, D., Periaux, J., Hirsch, C. and Pandolfi, M. John Wiley & Sons, Ltd. vol 2, pp. 694-703,* 1998.

[20] Dubuc, L., Cantariti, F., Woodgate, M., Gribben, B., Badcock, K.J., and Richards, B.E., "Solution of the Unsteady Euler Equations Using an Implicit Dual Time Method", *AIAA Journal, vol 36, No 8, pp. 1417-1427* 1998.

[21] Gnoffo, P.A., "Point-Implicit Relaxation Strategies for Viscous, Hypersonic Flows", *Computational Methods in Hypersonic Aerodynamics, edited by Murthy, T.K.S., Kluwer Acadamic Publishers, pp. 115-151,* 1993.

[22] Anderson, J.D., "Hypersonic and High Temperature Gas Dynamics", *McGraw-Hill Book Company, pp. 114-115,* 1989.

[23] Truitt, R.W., "Hypersonic Aerodynamics", *The Ronald Press Company, New York, pp. 231-296,*1959.

[24] Feszty, D., "Numerical Simulation of Steady Supersonic and Hypersonic Flows over Simple Bodies of Revolution", *Aero Report 9902, University of Glasgow,* February 1999.